NON-INVASIVE OPTICAL DETECTION OF EPITHELIAL CANCER USING OBLIQUE INCIDENCE DIFFUSE REFLECTANCE SPECTROSCOPY

A Dissertation

by

ALEJANDRO GARCIA URIBE

Submitted to the Office of Graduate Studies of
Texas A&M University
in partial fulfillment of the requirements for the degree of

DOCTOR OF PHILOSOPHY

May 2009

Major Subject: Electrical Engineering

NON-INVASIVE OPTICAL DETECTION OF EPITHELIAL CANCER USING OBLIQUE INCIDENCE DIFFUSE REFLECTANCE SPECTROSCOPY

A Dissertation

by

ALEJANDRO GARCIA URIBE

Submitted to the Office of Graduate Studies of
Texas A&M University
in partial fulfillment of the requirements for the degree of

DOCTOR OF PHILOSOPHY

Approved by:

Co-Chairs of Committee,	Jun Zou
	Lihong Wang
Committee Members,	Ohannes Eknoyan
	Andrew K. Chan
Head of Department,	Costas N. Georghiades

May 2009

Major Subject: Electrical Engineering

ABSTRACT

Non-invasive Optical Detection of Epithelial Cancer Using Oblique Incidence Diffuse Reflectance Spectroscopy. (May 2009)

Alejandro Garcia Uribe, B.S., Instituto Tecnológico de Morelia, Mexico
M.S., Texas A&M University

Co-Chairs of Advisory Committee: Dr. Jun Zou
Dr. Lihong Wang

This dissertation describes the design, fabrication and testing of an oblique incidence diffuse reflectance spectrometry (OIDRS) system for *in-vivo* and noninvasive detection of epithelial cancer. Two probes were fabricated using micromachining technology, which plays a significant role in the probe development by enabling device miniaturization, low-cost fabrication and precise assembly. The fist probe was developed and clinically tested for skin cancer detection. This probe consists of three source fibers, two linear array of collection fibers and four micromachined positioning devices for accurate alignment of the fibers. The spatially resolved diffuse reflectance spectra from 167 pigmented and 78 non-pigmented skin abnormalities were measured and used to design a set of classifiers to separate them into benign or malignant ones. These classifiers perform with an overall classification rate of 91%. The absorption and reduced scattering coefficient spectra were estimated to link the anatomic and physiologic properties of the lesions with the optical diagnosis. The melanoma cases presented larger average absorption and reduced scattering spectra than the dysplastic and benign ones. A second probe was designed to demonstrate the feasibility of a miniaturized “side viewing” optical sensor probe for OIDRS. The sensor probe consists of a lithographically patterned polymer waveguides chip and two micromachined positioning substrates. This miniaturize probe was used to measure twenty ex-vivo esophageal samples. Two statistical classifiers were designed to separate the esophageal cases. The first one distinguishes benign and low dysplastic from high dysplastic and cancerous lesions. The second classifier separates benign lesions from low dysplastic ones. Both classifiers generated a classification rate of 100%.

To my family, my mother Bertha, my father Luis Felipe, and my brothers Luis Felipe and Carlos Alberto

ACKNOWLEDGMENTS

I would like to express my sincere appreciation to Dr. Jun Zou and Dr. Lihong Wang for their guidance throughout my dissertation project and for giving me the opportunity to learn from them.

I would like to give my thanks to all my professors, friends, and all the staff at Texas A&M University. I gratefully acknowledge with thanks and extend my appreciation to Dr. Ohannes Eknoyan and Dr. Andrew K. Chan for being on my committee.

I want to especially thank my family, my mother, Bertha Uribe Madrigal, my father, Luis Felipe Garcia Tejeda, and my brothers, Luis Felipe Garcia Uribe and Carlos Alberto Garcia Uribe. Words cannot express how much I appreciate all your sincere encouragement and motivation. And part of my family that passed away while I was pursuing my graduate studies, Clementina Tejeda, and Maria del Carmen Gutierrez.

I thank the National Council of Science and Technology of Mexico (CONACyT) for sponsoring me during my doctoral studies.

I also want to thank all my closest friends for their sincere friendship during these years.

TABLE OF CONTENTS

LIST OF FIGURES

FIGURE Page

FIGURE Page

LIST OF TABLES

CHAPTER I

INTRODUCTION

Skin is a layered organ composed of the cellular, avascular epidermis and the less cellular, vascular collagenous dermis. Epidermal keratinocytes arise from stem cells in the basal layer. The basal layer of the keratinocytes interfaces with a basement membrane zone that distinctly separates the epidermal layer from the dermis. Although the epidermis is devoid of vessels, it is nourished by capillary loops in the upper dermis. The epidermis follows the irregular dermal surface forming an undulating pattern of rete ridges [1]. The dermis is composed of fibroblasts, connective tissue, vessels and epidermal appendages including hair follicles, eccrine, and sebaceous glands. There are also cells that traffic into the epidermis and dermis where they have specialized functions. These include epidermal melanocytes and langerhans cells and dermal white cells such as T lymphocytes, histiocytes, and neutrophils [1].

A. Skin Cancer

The most serious and deadly form of skin cancer is malignant melanoma. Melanomas account for most of the deaths from skin cancer. The American Cancer Society estimates that there are more than 62,000 new cases of melanoma in the United States every year. About 8,000 people are expected to die of this disease each year [2]. Early

---

This dissertation follows the style of *IEEE Sensors Journal*.

detection and treatment of skin cancer can significantly improve patient outcomes. Dyplastic nevi are skin tumors that have atypical size, shape, and organization of cells. Dysplastic nevi are generally considered to be precursors of melanoma [3]. Common nevi are benign growths formed by a cluster of melanocytes in the basal layer of the epidermis or the top layers of the dermis. Based on the location of the nests of melanocytes in the epidermis and dermis., these are junctional nevi, compound nevi and intradermal nevi.

Non-melanoma skin cancers are the most common cancers and include basal cell carcinomas and squamous cell carcinomas. The American Cancer Society estimates that there are 1.2 million new cases of non-melanoma skin cancers each year [2]. Squamous cell carcinomas (SCC) arise from dividing keratinocytes of the epidermis. They often arise from actinic keratoses (AK), which are characterized clinically by redness and scale. Squamous carcinomas are also often recognized by hyperkeratotic crusts or scales or by ulceration in the later stages. Squamous cell carcinomas may be aggressive and may metastasize to local nodes and beyond. When pigmented or rapidly changing or growing, seborrheic keratoses (SK) may also be mistaken for melanoma. Clinically, AKs, and SCC are difficult to distinguish from one another. Basal cell carcinomas (BCC) are thought to be derived from the keratinocytes and are characterized by islands or nests of basal keratinocytes invading the dermis. They are locally invasive, slow-growing tumors. There are several clinical and histologic subtypes of basal cell carcinomas. Superficial BCCs are papulosquamous lesions characterized by red, scaly raised plaques. Pigmented BCCs have a variegated appearance and can often be mistaken for melanomas.

B. Current Clinic Diagnostic of Skin Cancer

In clinical practice, dermatologists use the ABCD rule (asymmetry, border, color and diameter) and change in the appearance of a mole or pigmented area, to spot suspicious skin lesions. Melanomas usually are asymmetrical, have irregular borders, have color variation, and have a diameter greater than 6mm. Unfortunately, melanomas can also be perfectly symmetrical, have regular borders, be less than 6 mm in diameter and be of uniform color or no pigmented (amelanotic). After the skin check a skin biopsy is preformed for assessing whether the pigmented lesion is malignant or benign. Dermatoscopy, also called epiluminescent microscopy, uses a glass-oil interface to decrease the skin refraction. Dermatoscopy improves the resolution of the epidermal structures and increases a trained clinician's diagnostic accuracy. Confocal microscopy allows visualization of internal structures in the living skin, including blood flow [4].

C. Esophageal Cancer

The American Cancer Society estimates that cancer of the esophagus affects about 16,470 people with about 14,280 deaths each year in the United States [2]. Esophageal cancer is 3 to 4 times more common among men than among women. Because esophageal cancer is usually diagnosed at a late stage, most people with esophageal cancer eventually die of this disease. There are two main types of esophageal cancer: squamous cell carcinoma and adenocarcinoma. The esophagus is normally lined with squamous cells and most squamous cell cancers occur in the mid to proximal esophagus. Adenocarcinomas start in columnar tissue, which can be found in the distal esophagus. If Barrett's esophagus occurs in an intestinal area that previously contained squamous cells, it could develop into adenocarcinoma. Barrett’s esophagus occurs because of chronic gastroesophageal reflux from the stomach into the lower esophagus. If chronic gastroesophageal reflux is persistent, the acid and bile can produce injury to the lining of the esophagus, with specialized intestinal cells replacing the squamous cells that usually line the esophagus. People with Barrett’s esophagus are at an increased risk for developing cancer of the esophagus.

D. Current Clinic Diagnostic of Esophageal Cancer

Upper endoscopy is the most important tool for diagnosing esophageal cancer. It is a procedure involving the use of a gastroscope, which is one type of endoscope specially designed for gastroenterology applications. A biopsy can be taken through the endoscope for histology to determine whether cancer is present. People with strong risk factors for esophageal cancer should have periodic endoscopic biopsies. It is now recommended that the patient with Barrett's esophagus have four quadrant biopsies at every one or two centimeter intervals along the entire length of the Barrett's lining. The reason for taking four quadrant biopsies is that sampling all four walls of the esophagus decreases the odds of missing a small area of abnormal cells that can only be seen by histologic analysis and not through the endoscope. The current recommendation for patients who have a stable diagnosis of negative for dysplasia, confirmed by two endoscopic biopsy surveillance procedures, is that they come back every 3 years for follow-up endoscopic biopsy surveillance. For patients who have a stable diagnosis of low-grade dysplasia, confirmed by two endoscopic biopsy surveillance procedures, it is recommended that they return yearly for endoscopic biopsy surveillance until they have a set of biopsies in which no dysplasia is detected. All biopsies that reveal dysplasia are suggested to be submitted for re-interpretation by an expert pathologist due to problems with inconsistencies in interpreting histology. The intensive biopsy may also increase the chance of bleeding and discomfort to the patients. For these and other reasons, most patients who develop esophageal adenocarcinoma are not in a cancer surveillance program. As a result, endoscopic biopsy surveillance has not favorably impacted the mortality of this disease. In summary, esophageal cancers are very difficult to diagnose at the early and curable stage. Endoscopic surveillance is the only procedure to monitor possible development of esophageal cancers for people with strong risk factors. However, its effectiveness is largely hampered by the complexity and cost of the procedure, as well as possible complication and discomfort caused by the intensive biopsy. Sampling error of biopsy is also an issue. Although the use of more intensive biopsy protocols could reduce the sampling error, it inevitably results in even more complex and costly procedures. Therefore, it is highly necessary to investigate new endoscopic biopsy techniques to greatly reduce the complexity and cost of the surveillance procedures. The new biopsy techniques should be less invasive (to reduce the bleeding and discomfort), fast and simple to use [5].

E. Non-Invasive Optical Methods

Non-invasive methods for optical and spectroscopic methods for tissue diagnosis have been utilized for a number of organ systems, including the skin [6-15], gastrointestinal tract [16-20], cervix [21-24], and breast [25-27]. Much work has been done using fluorescence spectroscopy to detect incipient disease states on the premise that fluorescence, because it is a manifestation of the biochemical environment of the cell, should be a specific indicator of cellular alterations due to disease [28]. A number of recent reports have found that light scattering or reflectance measurements, either alone or in conjunction with fluorescence and Raman spectroscopy, are capable of distinguishing pathologic changes. It is likely that by restricting, or targeting, the area of tissue scanned by the light probe, either by appropriate selection of the incident wavelength or by the physical configuration of the light delivery and collection system, that the specificity of elastic scattering measurement systems can be improved. This approach partly overcomes one of the greatest perceived weaknesses of single-channel elastic scattering spectroscopy, i.e., that the fundamental optical properties of absorption and scattering are not individually resolved. Because of the highly turbid nature of biological tissues, the bulk optical transport properties of tissue may be only slightly changed by a localized pathological process, thus reducing the sensitivity of scattering and absorption as specific measures of disease. Therefore, it appears that further evaluation of scattering and reflectometry measurements may be productive for skin applications and other epithelial types of tissue. The measurement of tissue optical properties, such as scattering and absorption using diffuse reflectance, appears to be a useful approach for the detection of superficial lesions and generally involves simpler instrumentation than other optical methods.

CHAPTER II

OBLIQUE INCIDENCE DIFFUSE REFLECTANCE SPECTROSCOPY

A. Light Interaction in a Scattering and Absorbing Media

When light is incident on the surface of a semi-infinite (optically thick) medium (e.g. biological tissue), part of the incident light will be directly reflected (specular reflectance) and the remaining will transmit into and interacts with the media (Fig. 1).

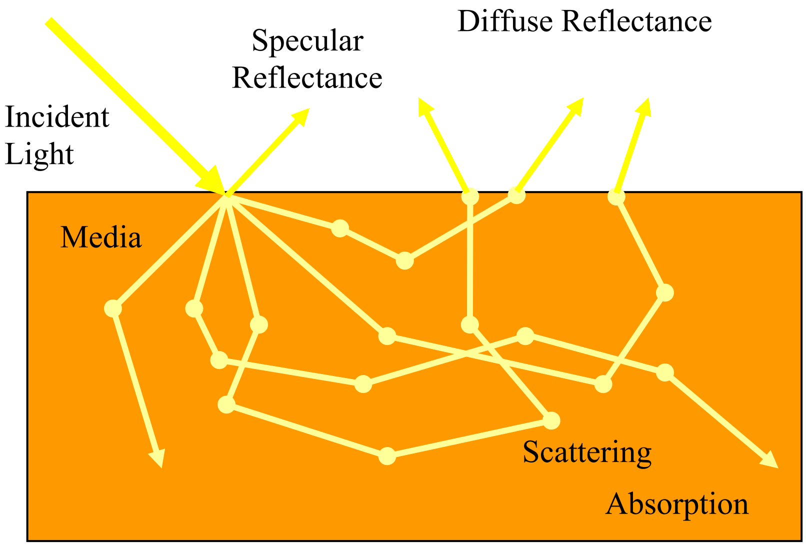

Fig. 1. Light interaction in a scattering and absorbing media.

Normal-incidence reflectometry can separate the two effects but only with absolute measurements of the multiple-scattered reflected light (diffuse reflectance), which are difficult to obtain reliably in a clinical setting. Different from normal-incidence reflectometry, OIDRS breaks the symmetry in the diffuse reflectance pattern. The Figs. 2 and 3 shows the diffuse reflectance pattern on the surface of a sample for normal and oblique incidence respectively.

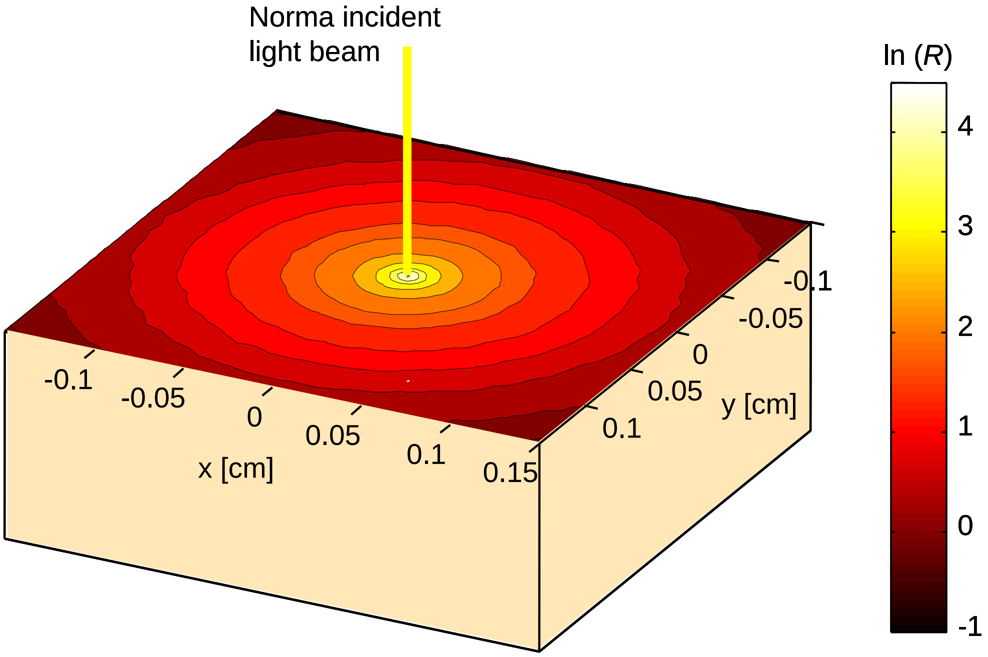

Fig. 2. Single wavelength normal incidence diffuse reflectance pattern.

The scattered light that escapes from the medium surface forms the diffuse reflectance. To characterize small section of the sample, the detectors used to collect the diffuse reflectance is placed in a fixed position close to the light source (e.g. 1~2 mm away). However, since the optical transport mean free path (L_t') is a function of the wavelength of the incident light, when a wide spectrum of light is used, the location of the detectors may fall within or outside the range of L_t' at different wavelength. When the detectors fall outside the range of L_t', the absorption and scattering optical properties of the medium can be directly calculated from the diffuse reflectance using a straightforward diffusion-theory based analytical model [29]. However, this model would fail in regions near the light source (e.g. within the range of L_t'). In this case, the Monte Carlo simulation can be conducted to deduce the absorption and scattering optical properties of the medium in an inverse problem by comparing and matching the simulation results with the actual measurements [30]. Monte Carlo simulation is very inefficient and slow when used in such iterative manner. An alternative is to the scaleable Monte Carlo method [31] in conjunction with the diffusion-theory based analytic model for the extraction of the absorption and reduced scattering properties from the diffuse reflectance spectra.

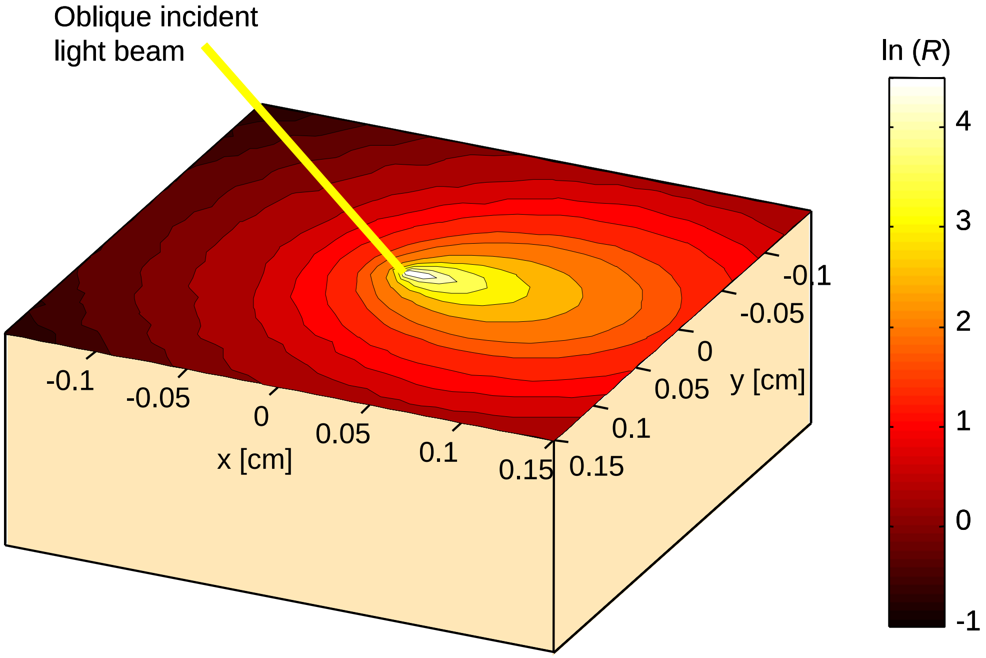

Fig. 3. Single wavelength oblique incidence diffuse reflectance pattern.

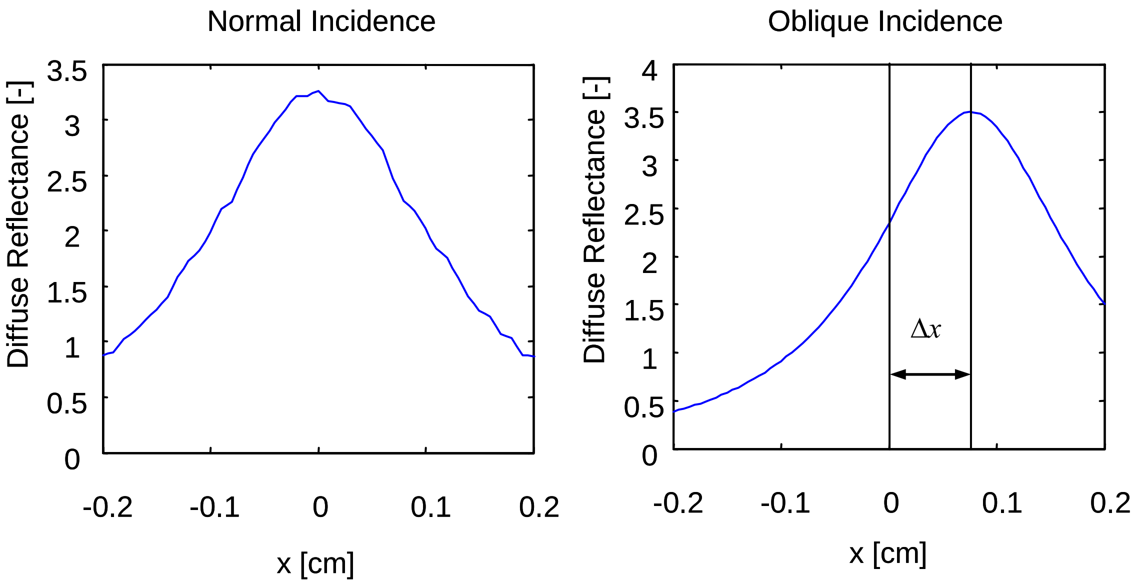

(a) (b)

Fig. 4. (a) normal incidence diffuse reflectance along the x direction for y=1.0 cm; (b) oblique incidence diffuse reflectance along the x direction for y=1.0 cm.

B. Diffusion Theory

The radiative transport equation (RTE) is an analytical model for photon transport in scattering and absorbing media such as biological tissues [32]. The RTE is an energy conservation equation for the radiance described by

$$\begin{aligned}\frac{1}{c}\frac{\partial L(\vec{r},\hat{s},t)}{\partial t} &= -\hat{s}\bullet\nabla L(\vec{r},\hat{s},t)-(\mu_a+\mu_s)[L(\vec{r},\hat{s},t)]+ \\ &+\mu_s\int[L(\vec{r},\hat{s}',t)p(\hat{s}'\bullet\hat{s})d\Omega']+S(\vec{r},\hat{s},t)\end{aligned} \tag{2.1}$$

where $L(\vec{r},\hat{s},t)$ is the radiance, which is defined as the amount of energy which, at position $\vec{r}$, flows per second through a unit area perpendicular to the unit vector $\hat{s}$. The parameters μ_a is the absorption coefficient, μ_s is the scattering coefficient and c is the velocity of light in the medium. The function $p(\hat{s}'\bullet\hat{s})$ is the scattering phase function. The product $p(\hat{s}'\bullet\hat{s})d\Omega$ represents the probability of being scattered into $d\Omega$ around the direction $\hat{s}$ given that it enters into the volume element from the direction $\hat{s}'$. The term $S(\vec{r},\hat{s},t)$ represents the source [33]. Although a general solution to the radiative transport equation is not easy to obtain analytically or numerically, a solution to the diffusion equation, a simplified version of the full transport equation under the diffusion approximation, can be found more easily. The diffusion equation is described by

$$\frac{1}{c}\frac{\partial\Phi(\vec{r},t)}{\partial t}+\mu_a\Phi(\vec{r},t)-D\nabla^2\Phi(\vec{r},t)=S(\vec{r},t) \tag{2.2}$$

where Φ is the fluence rate. The fluence rate Φ is the total radiance integrated over the entire 4π solid angle:

$$\Phi(\vec{r},t)=\int_{4\pi}L(\vec{r},\hat{s}',t)d\Omega \tag{2.3}$$

The parameter μ_s' is the reduced scattering coefficient and D is the diffusion coefficient defined by

$$D=\frac{1}{3(\mu_a+\mu_s')} \tag{2.4}$$

for the steady-state diffusion equation becomes:

$$\mu_a\Phi(\vec{r})-D\nabla^2\Phi(\vec{r})=S(\vec{r}) \tag{2.5}$$

for an isotropic point source $S(\vec{r})=\delta(\vec{r})$ in an infinite media the solution to steady-state diffusion equation is

$$\Phi(\vec{r})=\frac{1}{4\pi Dr}\exp\left(-\mu_{eff}r\right) \tag{2.6}$$

where the effective attenuation coefficient $\mu_{eff}=(\mu_a/D)^{1/2}$. The diffuse reflectance $R(r)$ on the surface of the semi-infinite scattering medium for an incident pencil beam can approach by converting it into a new problem of double sources in an infinite medium

$$R(r)=-D\left.\frac{\partial\Phi(r,z)}{\partial z}\right|_{z=0} \tag{2.7}$$

Normal-incidence reflectometry can separate the two effects but only with absolute measurements of the multiple-scattered reflected light (diffuse reflectance), which are difficult to obtain reliably in a clinical setting. Different from normal-incidence reflectometry, OIDRS breaks the symmetry in the diffuse reflectance pattern (Fig. 3). The spatially resolved steady-state diffuse reflectance for oblique incidence can be calculated using a modified two-source diffusion theory approximation with one positive source located below the sample surface and one negative located above the sample surface [34, 35]. The resolved steady-state diffuse reflectance a particular wavelength is described by

$$\begin{aligned}R_d(x)=(1-R_s)a'\frac{1}{4\pi}\Bigg[&\frac{\Delta z(1+\mu_{eff}\rho_1)\exp(-\mu_{eff}\rho_1)}{\rho_1^3}+\\&\frac{(\Delta z+2z_b)(1+\mu_{eff}\rho_2)\exp(-\mu_{eff}\rho_2)}{\rho_2^3}\Bigg]\end{aligned} \tag{2.8}$$

where ρ_1 and ρ_2 are the distances between the source point and the observation point on the skin surface. R_s is specular reflection, a' is albedo, and Δz is the distance between the virtual boundary and the tissue depth and z_b is the distance between the virtual boundary and the surface of the sample. The distance from the point of incidence to the positive point source $d_s = 3D$. For oblique incidence the diffusion coefficient is

$$D = \frac{1}{3(0.35\mu_a + \mu_s')} \tag{2.9}$$

the depth of the positive point source (Δz) is given by

$$\Delta z = 3D\cos(\alpha_t) \tag{2.10}$$

and the shift of the point sources in the x direction (Δx) is

$$\Delta x = \frac{\sin(\alpha_t)}{0.35\mu_a + \mu_s'} \tag{2.11}$$

where α_t is the angle of light transmission into the tissue (Figs. 5 and 6). Using simple geometrical transformations the absorption and reduced scattering coefficients can be calculated by

$$\mu_a = \frac{\mu_{eff}^2 \Delta x}{3\sin(\alpha_t)} \tag{2.12}$$

$$\mu_s' = \frac{\sin(\alpha_t)}{\Delta x} - 0.35\mu_a \tag{2.13}$$

The diffusion equation assumes that the reduced scattering coefficient is much larger than the absorption. The source and detector must also be separated in space to allow that the light is diffuse when it reaches the detector. Diffusion theory is accurate only when the distance between the source and the detectors is comparable to the transport mean free path L_t'.

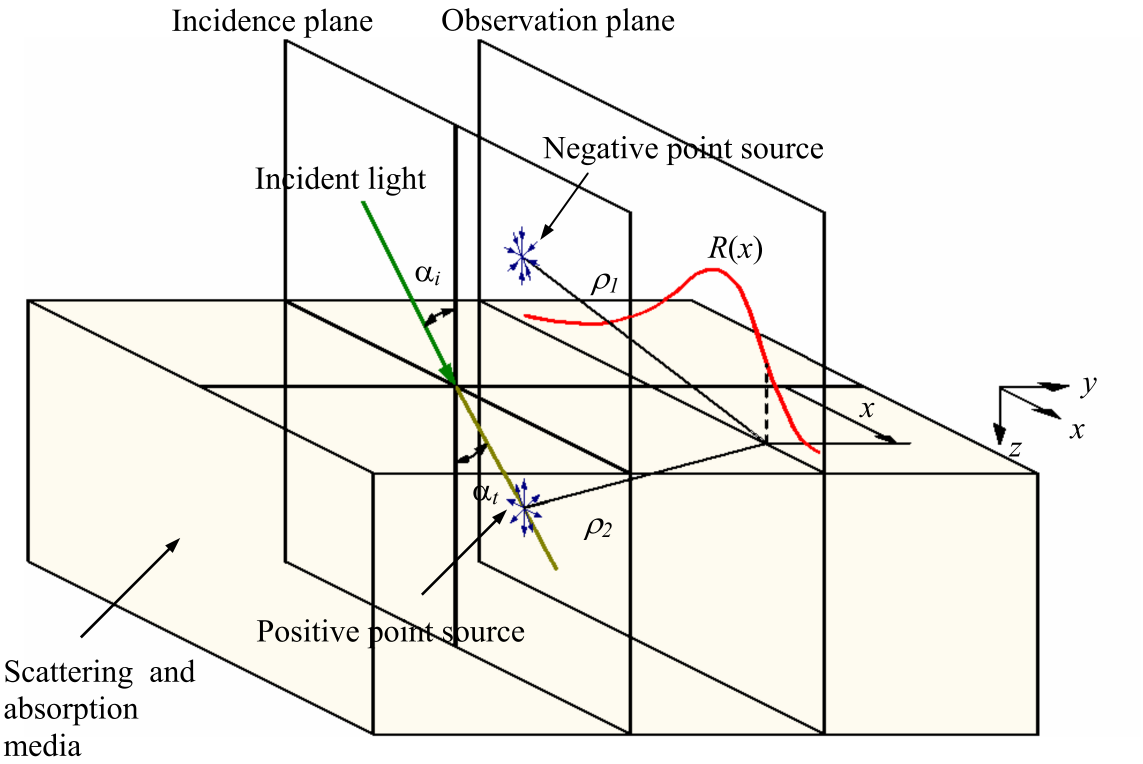

Fig. 5. Schematic of the modified two-source approximation of oblique incidence based on diffusion theory.

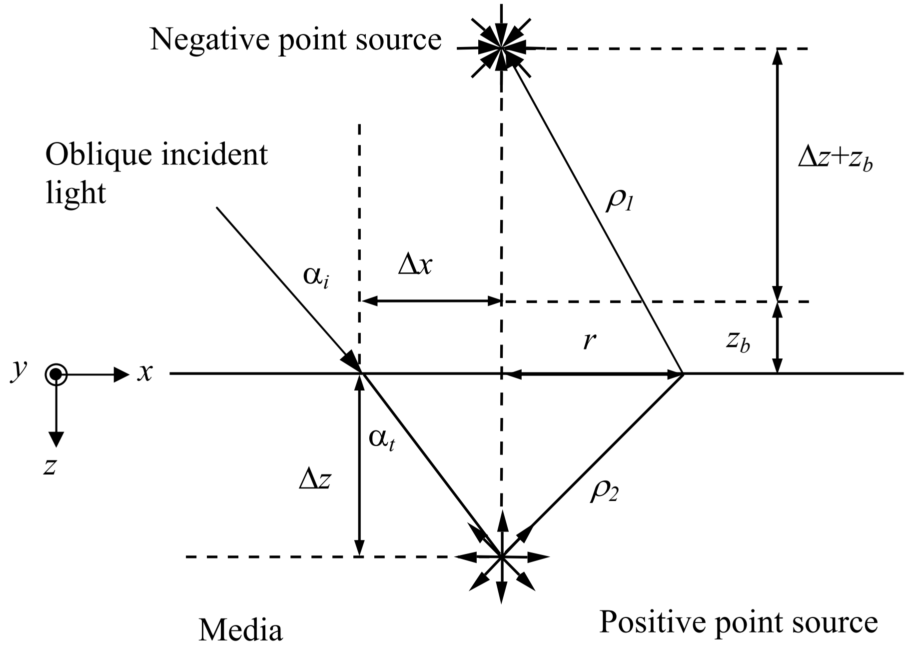

Fig. 6. Schematic of the incidence plane.

C. Scaleable Monte-Carlo

The diffusion theory model cannot accurately predict the diffuse reflectance near to the source (before the diffusion regime). This problem can be solved by using scaleable Monte-Carlo for these cases. First, a single reference initial Monte Carlo simulation was run with a fixed anisotropy factor *g*. [36-42]. The scaleable simulation is possible because the Monte Carlo simulation results for given reference values of the index of refraction (*n)*, anisotropy factor (*g)*, absorption coefficients (μ_a) and scattering coefficient (μ_s) can be used to calculate the diffuse reflectance for a different set of absorption coefficients by applying Beer's law. The results may also be scaled for all scattering coefficients (μ_s) while n and g are held constant because different μ_s values change only the distances between the interaction points on the photon paths through the tissue. Kienle and Patterson [43] demonstrated that different anisotropy factors do not significantly influence the reflectance if g is close to unity ($g > 0.8$) as long as μ_a and μ_s' are the same. For biological tissue, g is usually greater than 0.9. We will initially fix g at 0.9 in the single Monte Carlo simulation. If the time-resolved diffuse reflectance $R_r(x, y, t)$ computed for reference parameters μ_{ar} and μ_{sr} is obtained using a single Monte Carlo simulation, the time-resolved diffuse reflectance $R(x, y, t)$ for any new parameters, μ_a and μ_s', and the corresponding steady-state diffuse reflectance, can be calculated by

$$R(x,y,t)=\left(\frac{\mu_s}{\mu_{sr}}\right)^3 R_r\left(x\frac{\mu_s}{\mu_{sr}},y\frac{\mu_s}{\mu_{sr}},t\frac{\mu_s}{\mu_{sr}}\right)\cdot\exp\left[-(\mu_a-\mu_{ar})\frac{\mu_s}{\mu_{sr}}ct\right] \qquad (2.13)$$

where c is the speed of light in vacuum and n is the index of refraction of the tissue. The pre-calculated results from the single Monte Carlo simulation for the reference parameters will be saved in a computer file. $R(x, t)$ is obtained by first scaling in the y direction. The corresponding steady-state diffuse reflectance is calculated by

$$R(x)=\int_0^\infty R(x,t)dt \qquad (2.14)$$

The above equation for $R(x)$ is used to fit the experimentally measured diffuse reflectance. We will repeat this process for different values of g in the range form 0.7 to 0.95 to obtain the best estimate for the optical properties.

The selected Monte-Carlo technique used the is the delta-scattering for photon tracing [41, 44]. Drs. Lihong Wang and S. L. Jacques developed a Monte Carlo software for modeling photon transport in biological tissues [41]. This software has been used in this dissertation for predicting the light distribution in biological tissue. The algorithm is briefly summarized in [45] as follows:

The interaction coefficient of the *i*th tissue type, defined as the sum of μ_a and μ_s, is denoted by μ_i.

1. Define an upper-bound interaction coefficient μ_m, where $\mu_m \geq \mu_i$ for all i. In this study, μ_m was set to the maximum μ_i among all tissue types.

2. Select a step size R between two consecutive interactions based on the upper-bound interaction coefficient: $R = -\ln(\xi_R) / \mu_m$, where ξ_R was a uniformly distributed random number between 0 and 1 ($0 < \xi_R \leq 1$). Then, determine the tentative next collision site $\mathbf{r}_k'$ by $\mathbf{r}_k' = \mathbf{r}_k\text{-}1 + R\ \mathbf{u}_k\text{-}1$, where $\mathbf{r}_k\text{-}1$ was the current site, and $\mathbf{u}_{k\text{-}1}$ was the direction of the flight. The direction of the flight was determined according to the probability distributions of the deflection (polar) angle and azimuth angle at each interaction site.

3. Play a rejection game: Get another random number ξ_a, which was uniformly distributed between 0 and 1 ($0 < \xi_a \leq 1$).

a. If $\xi_a \leq \mu_i(\mathbf{r}_k')/\mu_m$, i.e., with a probability of $\mu_i(\mathbf{r}_k')/\mu_m$, accept this point as a real interaction site ($\mathbf{r}_k = \mathbf{r}_k'$).

b. Otherwise, do not accept $\mathbf{r}_k'$ as a real interaction site but select a new path starting from $\mathbf{r}_k'$ with the unchanged direction $\mathbf{u}_k\text{-}1$ (i.e., set $\mathbf{r}_k\text{-}1 = \mathbf{r}_k'$ and return to

Step 2).

At each real interaction site, a fraction $\mu_a/(\mu_a + \mu_s)$ of the photon packet is absorbed, and the rest is scattered.

CHAPTER III

EXPERIMENTAL SYSTEM

A. Sensor Probe Design

To conduct OIDRS measurement on human skins, we have developed a hand-held fiber optical sensor probe to facilitate convenient and robust data collection in a clinical environment (Fig. 7). The main parameters to consider are:

1) Center-to-center distance between detectors (collection fibers): the center-to-center distance is critical to ensure a suitable spatial density of the detectors to capture the profile of the diffuse reflectance for the extraction of optical absorption and scattering properties.

2) Source-detector distance: Since the diffuse reflectance signal decreases rapidly away to the source. The detector array should be placed close to the source to increase the signal to noise ratio (SNR).

3) Number of detectors: Increasing the number of detectors is expected to collect more useful optical information, however at the expense of more complex system. The number or detector that can be couple to the input port of the imaging the spectrograph is limited to 20.

4) Diameter of the collection fibers the area of the detector of proportional to the amount of light collected from the surface of the sample, increasing the signal to noise ratio. But a larger collection fiber would reduce the number of them that can be used in the imaging spectrograph.

The 100 μm collection arrays provides good signal to noise ratio. The center-to-center distance of 100 μm, ensures the need resolution of the profile of the diffuse reflectance to calculate the optical properties.

The sensor probe consists of three source fibers and two linear arrays of collection fibers for capturing the spatial distribution of diffuse reflectance ($R_d(x)$). The effective probe testing area is limited to 2×2 mm^2 to ensure that the measured area does not include the surrounding normal skin even for the smallest skin lesions. Among the three source fibers, two are used for oblique incidence (delivering light onto the skin surface at an oblique angle (α) of 45^o. Since the OIDRS measurement is usually performed in a dark environment to reduce the effect of the background light, the center normal incidence source fiber is used to illuminate area of interest on the skin to ensure the accurate placement of the sensor probe. Although only one oblique incidence fiber and one linear array of collection fibers are necessary for an OIDRS measurement, two oblique incidence fibers and two arrays of collection fibers are used for multiple data collections from the same location on the skin to ensure a reliable and robust measurement [46, 47].

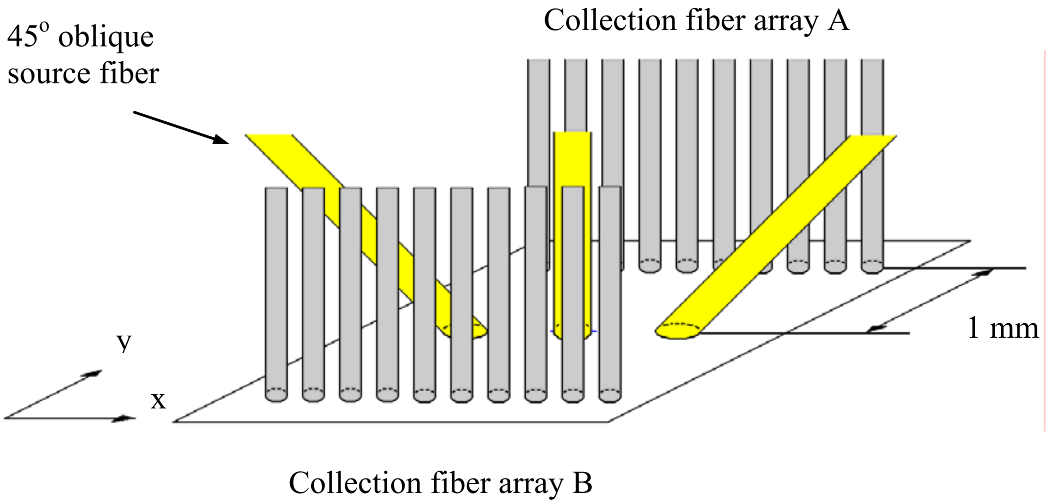

Fig. 7. Schematic design of the OIDRS probe.

For the source fibers, optical fibers with a diameter of 200 μm are used to provide enough incident light to ensure high signal-to-noise ratio (SNR) of the measurement, especially for dark-color skins. For the collection fibers, each of the two linear arrays consists of 10 fibers with a diameter of 100 μm and a center-to-center pitch of 200 μm. Based on our previous simulation, at least 10 data points are needed for a span of 2 mm to achieve a good spatial resolution for the estimation of the optical absorption and scattering properties with good accuracy. The 100 μm diameter of the collection fibers is expected to provide satisfactory SNR for the measurement of diffuse reflectance. The use of smaller collection fibers will result in lower SNR and the use of bigger collection fibers would unnecessarily increase the size of the probe or lower the spatial resolution of data sampling. The two collection fiber arrays are separate from the incidence fibers by 1 mm. This is because the estimation of the absorption and scattering coefficients from the measured diffuse reflectance is based on the Diffusion Theory, which is accurate only when the distance between the detector and the source is greater than one mean free path $Lt' = 1/(\mu_a+\mu_s')$, typically about 0.1 cm for biological tissues [32]. Although larger separation could be used, it will unnecessarily increase the overall size of sensor probe.

B. Sensor Probe Fabrication

To ensure the accuracy of the OIDRS measurements, the source fibers and collection fibers need to be precisely aligned with respect to each other and fixed in their own positions. This can be achieved with a compact mechanical positioning device. However, due to the small size and dense arrangement of the fibers, it is very difficult and costly to fabricate the mechanical positioning device using conventional machining methods. To address this issue, we have developed straightforward micromachining processes to achieve successful fabrication of the positioning devices in an efficient and low-cost manner.

To achieve accurate alignment of the collection fibers, two micromachined positioning devices were fabricated. Each positioning device consists of a silicon substrate with a linear array of V-grooves created with silicon bulk etching (Fig. 8). When an optical fiber (with cylindrical cross-section) is placed in a V-groove, the center axis of the optical fiber can "automatically" align with the symmetric plane of the V-groove. Thus, the accurate positioning of each collection fiber in the array can be readily achieved to ensure reliable and uniform performance of the sensor probe. To fabricate the positioning device, silicon nitride was deposited on a {100} silicon wafer. Photolithography and reactive ion etching was conducted to pattern the silicon nitride layer, which serves as a hard mask for silicon bulk etching. Silicon bulking etching was performed in potassium hydroxide solution to form the V-grooves (130μm wide and 200 μm apart).

For aligning the source fibers, two other micromachined positioning devices were fabricated. Since the need of guiding structures for the oblique incidence fibers (45^{o}) precludes the fabrication of V-grooves with silicon bulk etching, SU-8 resist (MicroChem, MA) was used for the fabrication of the guiding structures on a silicon substrate (Fig. 8). SU-8 is preferable for this process as it can be directly used to form structures over 100 μm in thickness, which results in a very simple and low-cost fabrication process. To fabricate the SU-8 guiding structure, a silicon substrate is first cleaned and backed at 200^{o}C for 5 minutes. SU-8 100 resist was spun on the cleaned silicon substrate at calibrated spinning rate for 40 seconds to reach a final thickness of about 100 μm. A soft bake was conducted at 65^{o}C for 10 minutes and then at 95^{o}C for 30 minutes, which was followed by a UV (ultraviolet) exposure of a dosage of about 520 mJ/cm^2. After the exposure, the wafer was baked at 65^{o}C for 1 minute and then at 95^{o}C for 10 minutes to selectively cross-link the exposed part of the SU-8 film. The development of exposed SU-8 film was conducted for a few minutes until unexposed region was completely removed. During the SU-8 processing, a slow temperature ramping was used to minimize the internal stress build-up and also the resulting crack formation within the SU-8 film, which would significantly reduced the mechanical strength and stability of the guiding structures.

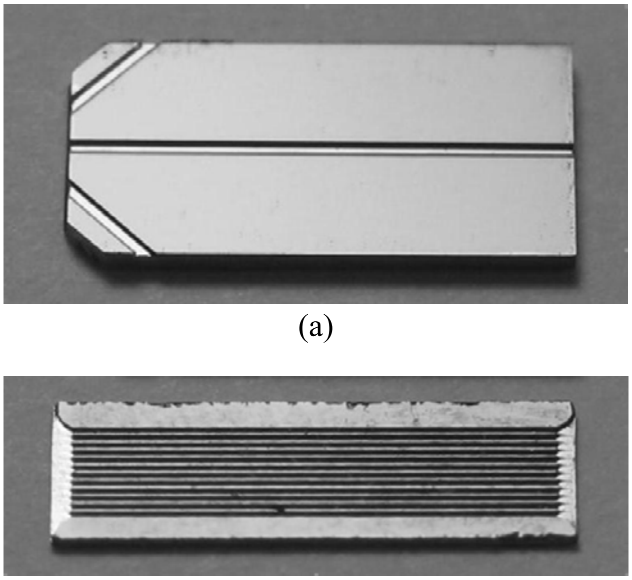
(a)

(b)

Fig. 8. Micromachined positioning devices for alignment and assembly of optical fibers in the OIDRS probe: (b) For the incidence fibers; (a) For the collection fibers.

After the fabrication of the micro positioning devices was complete, the entire OIDRS sensor probe was assembled. First, both the source and collection fibers were fixed into their own guiding structures (Fig. 9). Since the thickness of the SU-8 guiding structure is 100 μm, two positioning devices were placed face-to-face to accommodate the source fibers (with a diameter of 200 μm). For the collection fibers, one positioning device and one cover substrate were used to hold them in place. After all the fibers were assembled, the positioning devices were stacked and glued together with epoxy (Fig. 10).

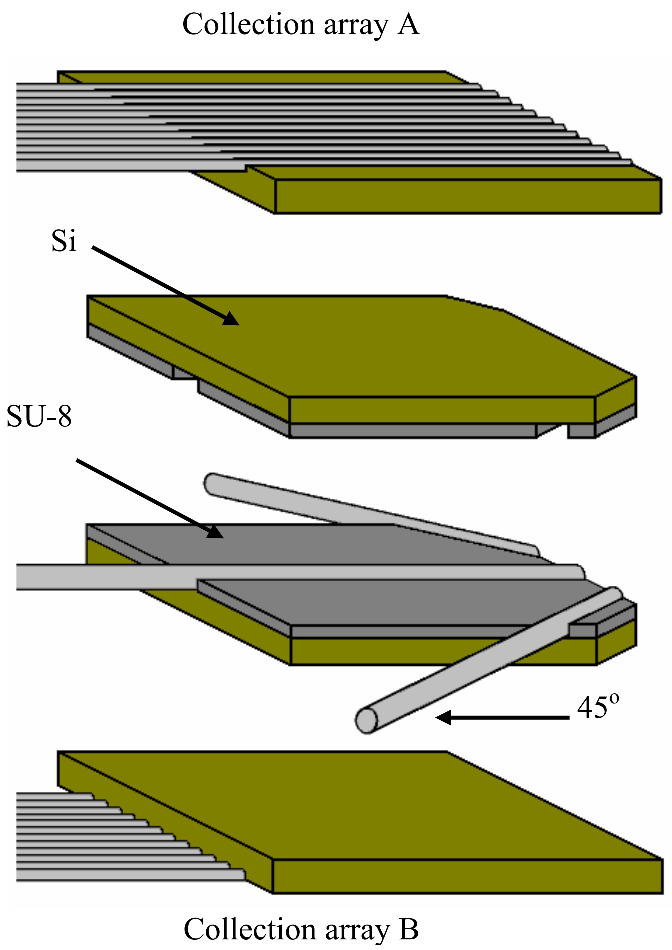

Fig. 9. Probe assembly.

Since the thickness of the silicon wafer used for the fabrication of the positioning devices is around 500 μm, the required 1 mm spacing between the source and collection fibers were readily obtained. To improve the efficiency of incidence and collection of the fibers, the head of the assembled probe was polished with sand papers. During the polishing, care was taken to avoid any possible damage to the fibers. Finally, the assembled probe was placed in an aluminum probe holder for testing (Fig. 10).

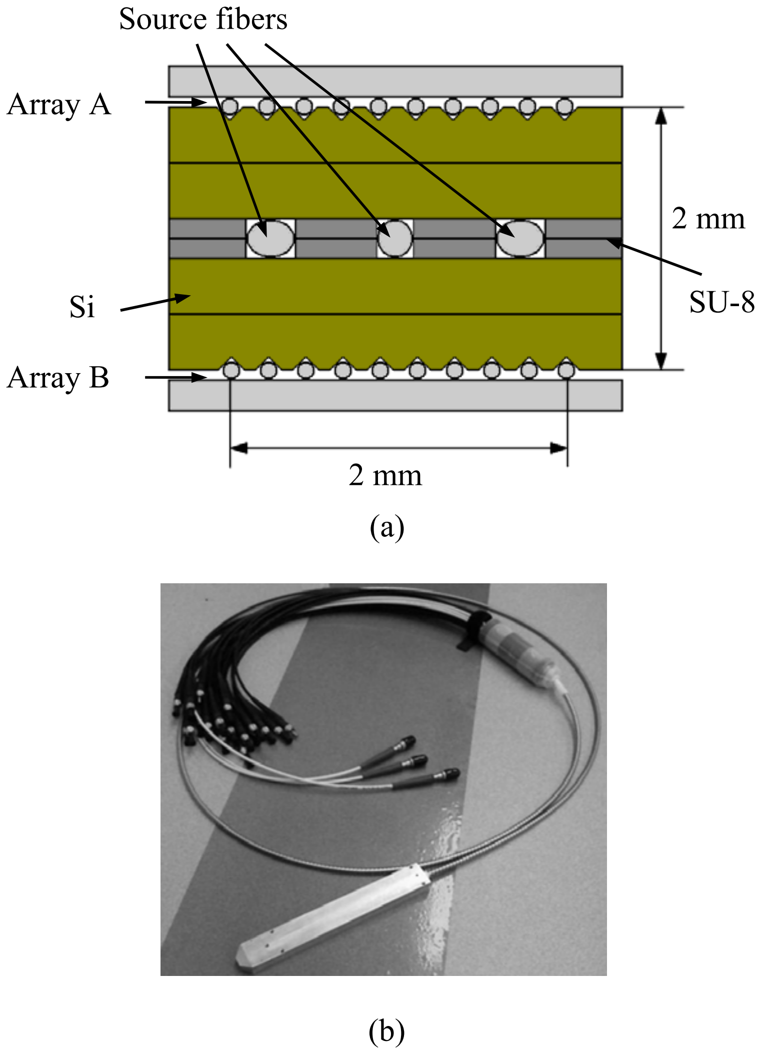

Fig. 10. (a) Schematic of the probe front view. (b) Complete probe.

C. Experimental Setup

The complete experimental setup consists of white light source (halogen lamp) for multiple-wavelength measurement, multiplexer, imaging spectrograph, CCD camera, and personal computer (Fig. 11). Before an OIDRS measurement is conducted, the three source fibers of the sensor probe are connected to the output of the light source via SMA connectors. The proximal end of each collection fiber is fitted with SMA 905 connectors and then connected to the input of the spectrograph through a custom-made interface. The optical multiplexer allows the light delivery, to the area of interest, through only one source fiber at a time. After the sensor probe gets into contact with the skin, white light is delivered through one of the source fibers and the diffuse reflectance is then captured by the collection fibers. The collection fibers are coupled with the imaging spectrograph that generates an optical spectrum for each fiber. The CCD camera collects the spectral-images from the wavelength range of 455 to 765 nm. The spectral images represent the steady-state diffuse reflectance spectra from each collection fiber, which are stored in the computer for further analysis. This system is capable of capturing one frame of spectral image in a fraction of a second.

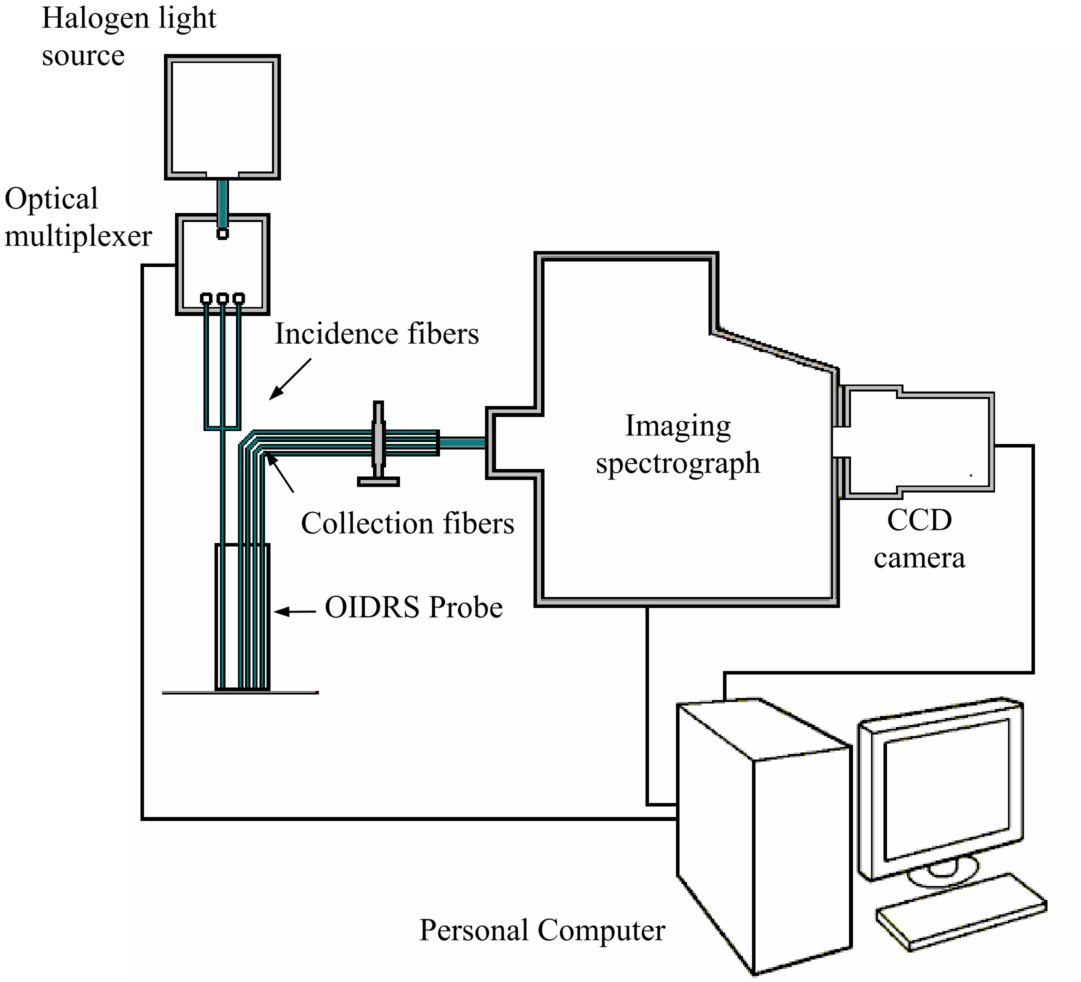

Fig. 11. Schematic of the oblique incidence diffuse reflectance spectroscopy system.

Before the actual OIDRS measurement was conducted, the entire system was calibrated using a liquid reference solution (phantom) consisting of polystyrene microspheres as scattering elements and Trypan blue as absorber [48].

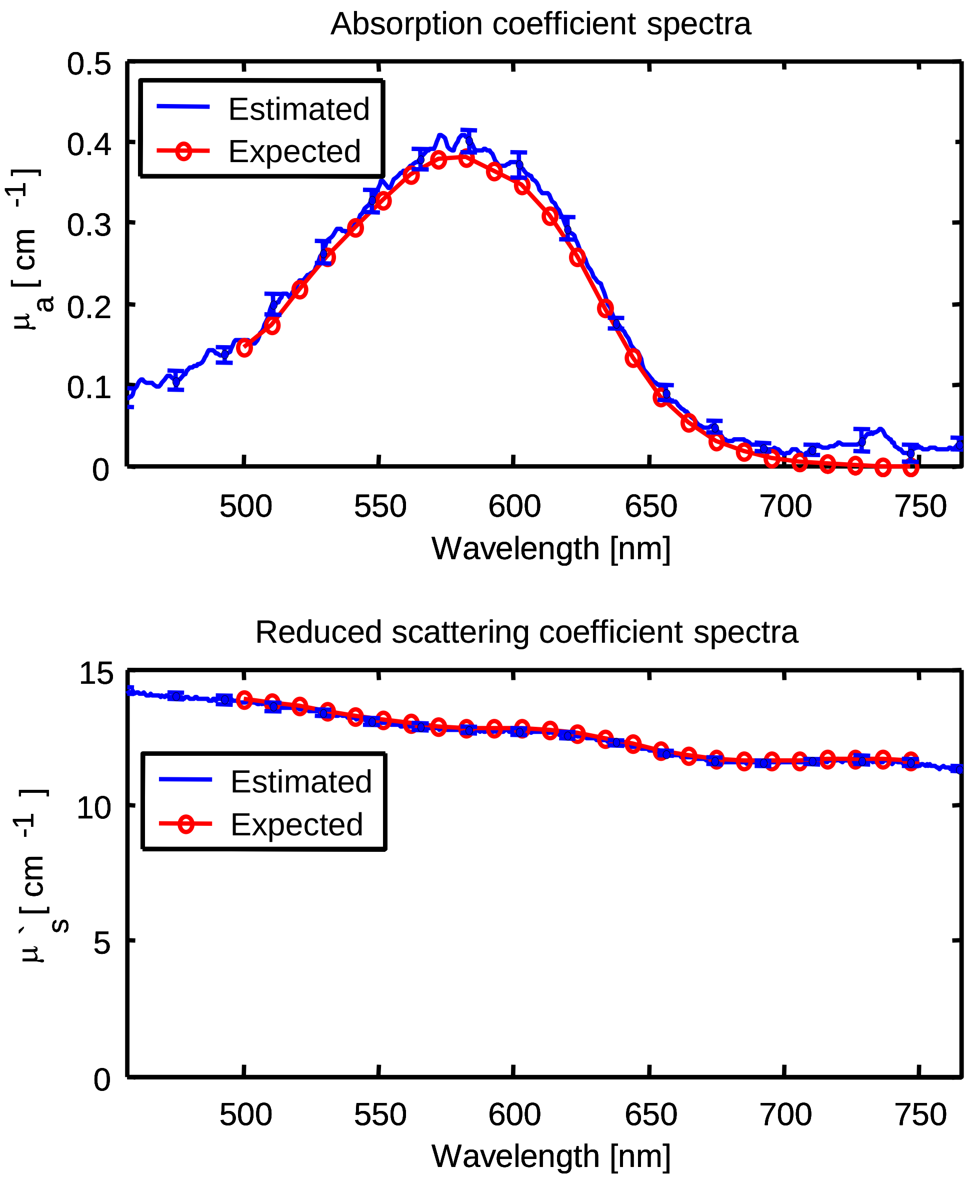

Fig. 12. Expected and estimated absorption and reduced scattering spectra of a liquid reference solution.

The absorption coefficient spectra of trypan blue were measured by collimated transmission before mixing it with the polystyrene micro-spheres. The reduced scattering coefficient of the microspheres was calculated using the Mie theory [49]. The "expected values" of the absorption and reduced scattering coefficients of the liquid reference solution can be varied by controlling the concentration of absorbing and scattering chemicals. To conduct the calibration, the sensor probe was placed on the surface of the reference solution. The absorption and reduced scattering spectra were extracted for each diffuse reflectance measurement and averaged to obtain the "estimated values". The system was calibrated by measuring several optical reference phantoms. Each collection channel is compensated by a k-factor (transmission) that matches the "estimated" diffuse reflectance to their expected values [48]. Fig. 12 shows the system validation by comparing the expected and estimated absorption and reduced scattering spectra of a liquid optical reference solution.

D. *In-Vivo* Measurement of Optical Properties

The OIDRS system is used to collect the steady-state spatially resolved diffuse reflectance spectra $R_d(x, \lambda)$ from human skin on the arm (Fig. 13). The main absorbers of human skin are hemoglobin and melanin. The extinction coefficients of melanin oxy-hemoglobin and deoxy-hemoglobin are shown in Fig. 14.

The extinction coefficient is the absorbance (of light) per unit path length and per unit of concentration (cm^{-1} $mMoles^{-1}$). The lower reflectance points at the wavelengths 550 and 575 nm correspond to local stronger absorption caused by oxy-hemoglobin [50].

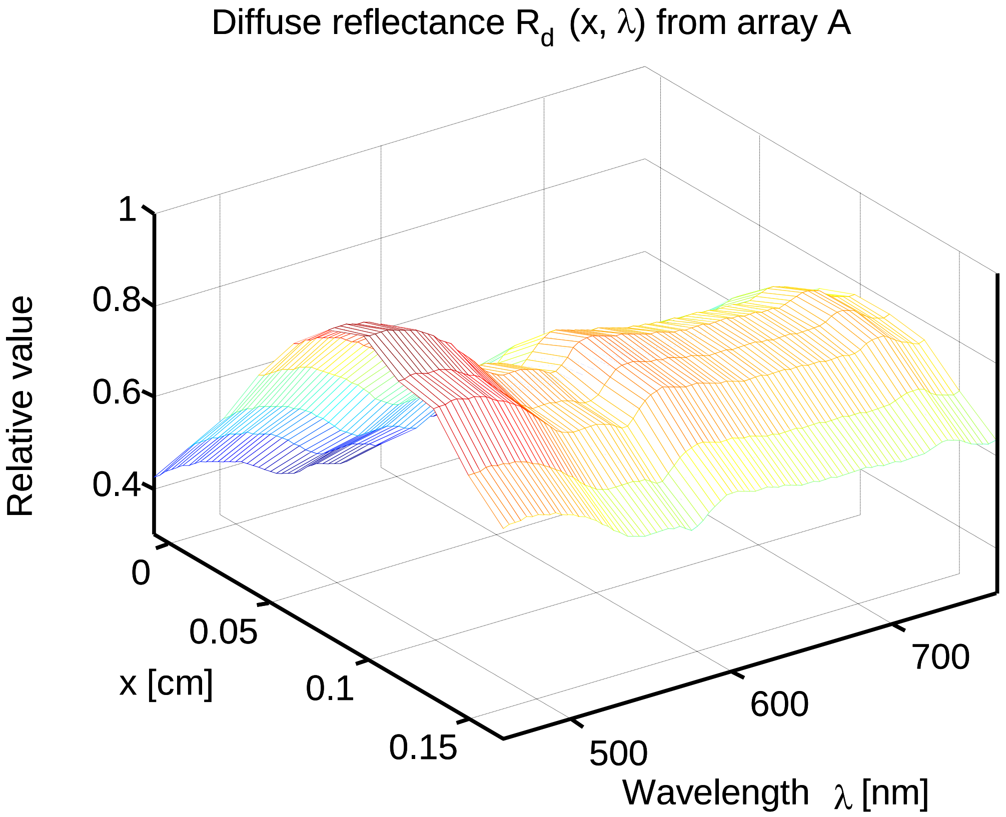

Fig. 13. Sample spatio-spectra diffuse reflectance data collected from human skin.

The absorption and scattering coefficients are calculated independently for each wavelength λ, using the corresponding diffuse reflectance along the *x* axis. An example of the estimated absorption coefficient spectra $\mu_a(\lambda)$ and scattering coefficient spectra $\mu_s'(\lambda)$ are shown in Fig. 15.

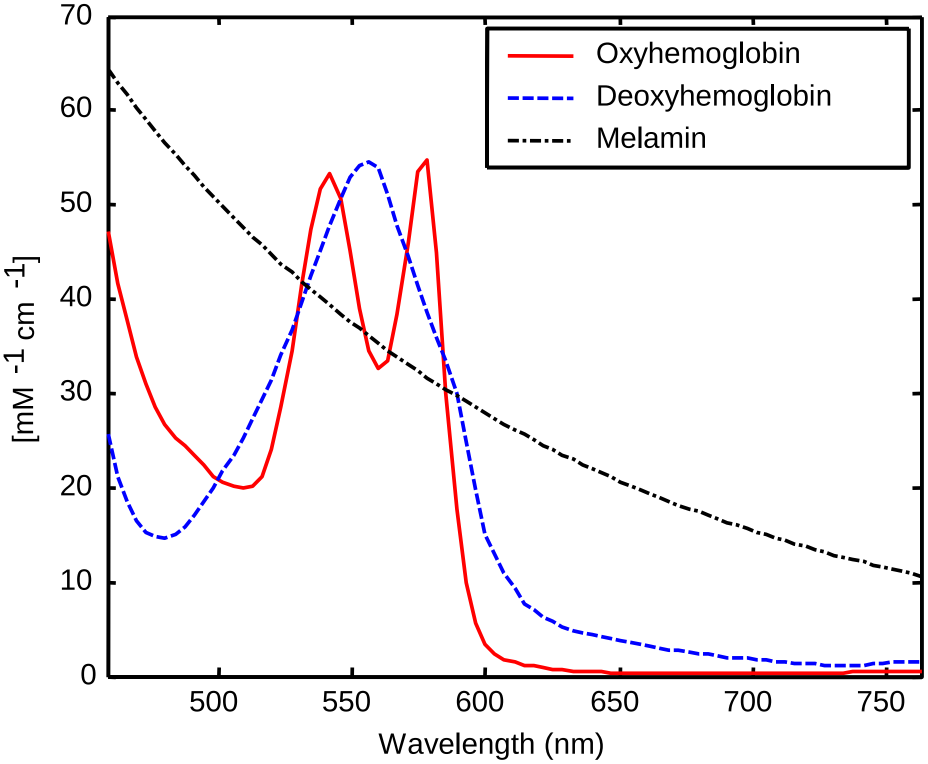

Fig. 14. Extinction coefficient of oxyhemoglobin, deoxyhemoglobin and melanin. The spectral difference between the two forms of hemoglobin can be used to assay the blood oxygen saturation by computing the relative concentration values of the two forms.

The optical properties of the skin can differ largely depending on race, age, and location on the body [51]. Our results match closely with those obtained previously in ex-vivo measurements presented in [52, 53] and the *in-vivo* measurements presented in [54].

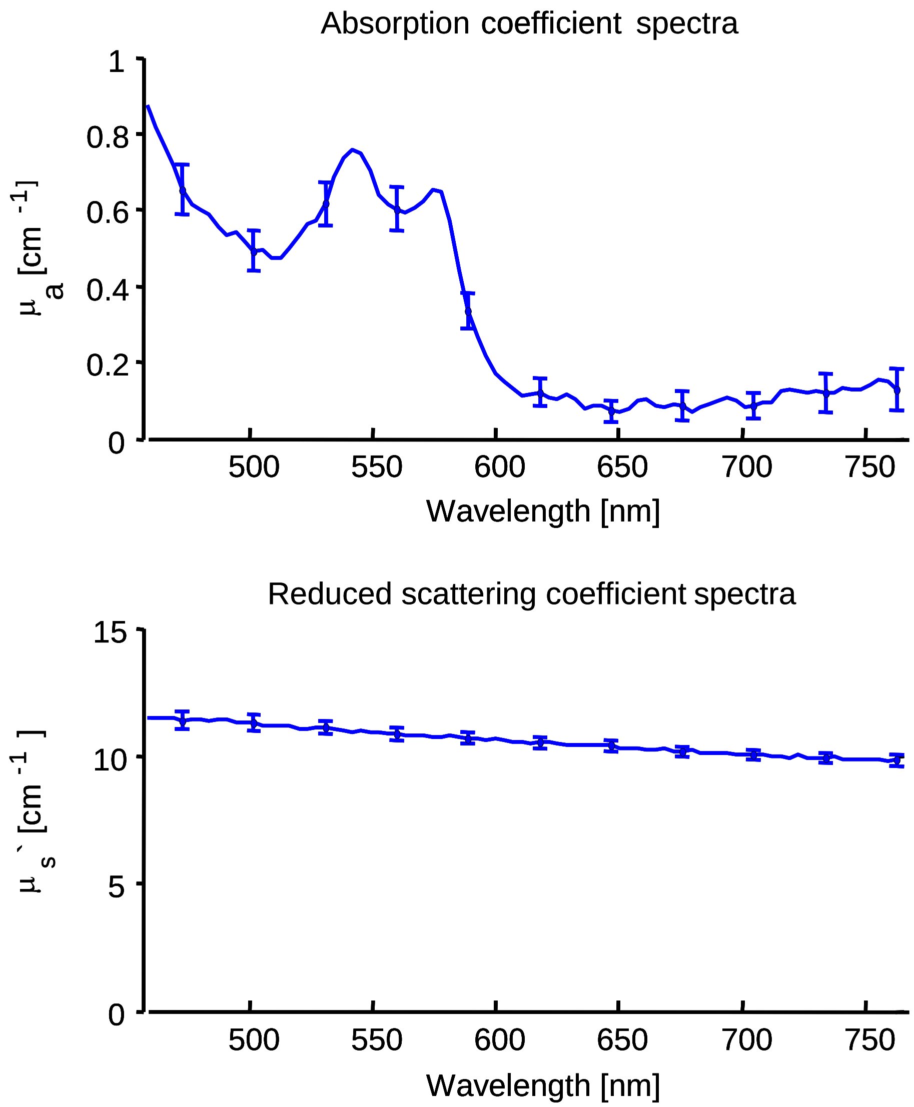

Fig. 15. Example of the estimated absorption and scattering coefficient from human skin.

The absorption coefficient can be used to estimate important physiological parameters related to the disease state such as the concentration of oxy-hemoglobin, deoxy-hemoglobin and its oxygen saturation (StO_2) [55]. For example, the absorption spectra $\mu_a(\lambda)$ is related to the concentration of the absorbers by

$$\mu_a(\lambda) = \varepsilon_{oxy}(\lambda)C_{oxy} + \varepsilon_{deoxy}(\lambda)C_{deoxy} + \varepsilon_{mel}(\lambda)C_{mel} + \mu_{abg} \qquad (3.1)$$

where $\varepsilon_{oxy}(\lambda)$, $\varepsilon_{deoxy}(\lambda)$, and $\varepsilon_{mel}(\lambda)$ are the known extinction coefficients of oxy-hemoglobin, deoxy-hemoglobin, and melanin at certain wavelength (λ), C_{oxy}, C_{deoxy}, and C_{mel} are the concentrations (mMoles) of oxy-hemoglobin, deoxy-hemoglobin, and melanin, and μ_{abg} is the absorption caused by other local tissue components. The oxygen saturation (StO_2) can be determined as

$$StO_2 = C_{oxy} /(C_{oxy} + C_{deoxy}) \qquad (3.2)$$

For the example provided in Fig. 15, the estimated concentrations are C_{oxy}=0.0063 mMoles, C_{deoxy}=0.0038 mMoles with an oxygen saturation StO_2=0.62%.

CHAPTER IV

SKIN CANCER DETECTION

The human skin is a heterogeneous media and its optical properties can vary significantly even between close sites. Recent study has suggested the close relationship between the stage of skin diseases (e.g. skin cancers) and the optical (absorption and scattering) properties of the affected skin area [56-59]. Thus, the development of *in-vivo* methods to accurately characterize localized optical properties of human skins can potentially assist in the diagnosis and treatment of its diseases [60-62]. Skin cancer is the most common form of cancer, with about a million new cases estimated in the U.S. each year [2]. Melanoma is the most dangerous type of skin cancer and is the leading cause of death among the skin diseases.

A. OIDRS Image Database

The data collection was performed at the University of Texas M.D. Anderson Cancer Center in Houston. First, the physician would identify the lesion(s) of interest scheduled for biopsy. The measurement from each lesion was repeated four times, the probe was repositioned to obtain images from different locations and orientations to average out the effect of structural anisotropy. This process was repeated for the neighboring healthy skin. The collected OIDRS images were divided into two abnormality groups. The pigmented group included the following two cancerous, dysplastic and benign subgroups:

(1) melanoma in situ and invasive melanoma (M).

(2) mild dysplastic nevi (DN1), moderate dysplastic nevi (DN2), severe dysplastic nevi (DN3).

(3) common Nevi,(CN), actinic keratosis (AK,) seborrheic keratosis (SK).

The non-pigmented group consisted of the following two cancerous and benign subgroups:

(1) basal cell carcinomas (BCC) and squamous cell carcinomas (SCC).

(2) actinic keratosis (AK,) seborrheic keratosis (SK).

Data was collected from 167 pigmented and 78 non-pigmented skin lesions. The pigmented group includes 16 lesions histopathologically diagnosed as melanoma. Tables I and II show types and number of lesions for the pigmented and non-pigmented group respectively.

Table I. Pigmented skin lesions.

Type of lesion	#
Melanoma (M)	16
Severe dysplastic nevi (DN3)	8
Moderate dysplastic nevi (DN2)	61
Mild dysplastic nevi (DN1)	30
Common nevi (CN)	31
Actinic keratosis (AK)	5
Seborrheic keratosis (SK)	16
Total	167

Table II. Non-pigmented skin lesions.

Type of lesion	#
Basal cell carcinoma (BCC)	35
Squamous cell carcinoma (SCC)	21
Actinic keratosis (AK)	17
Seborrheic keratosis (SK)	5
Total	78

B. OIDRS Image Analysis

OIR Image analysis was performed to identify those image features that differed significantly for cancerous and benign abnormalities. It should be noted that due to the highly nonlinear relationship between image features and optical properties, a difference in image features should not be interpreted to mean the same level of difference in optical properties. In our first preliminary analysis, we concentrated on identifying the differences in image features, not those in optical properties. In our second preliminary analysis, presented in Section C5, we examined differences in physiological properties.

The following steps were involved in the analysis of the spatio-spectral images: 1) Image preprocessing to remove noise and artifacts; 2) Extraction of various image features; 3) Feature selection to obtain effective image features; 4) Feature conditioning to combine all effective image features into one image feature; 5) Classification to categorize different abnormalities based on the combined image feature.

C. Data Preprocessing

Before each OIDRS image was stored, background subtraction was performed to remove the dark room camera system noise. The filtered spatio-spectral images were then calibrated against the k-factor (transmission correction) of each fiber. Appropriate k-factors were determined by matching the measured reflectance profile of a phantom with known optical properties to the theoretical profile at a particular wavelength [63]. Fig. 16 shows a typical spatio-spectral OIDRS image.

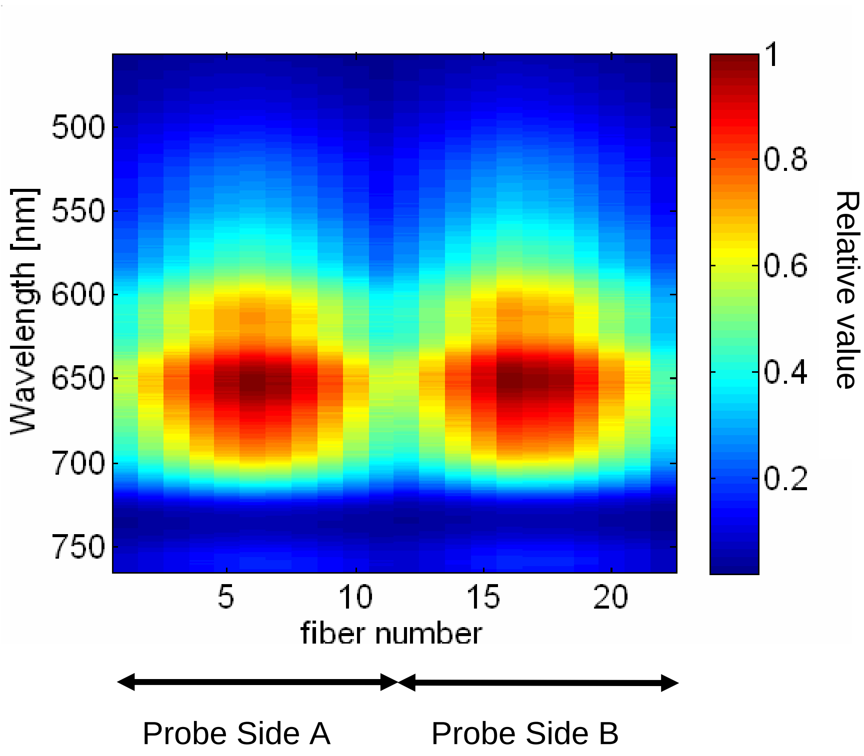

Fig. 16. A sample spatio-spectral OIDRS image before normalization.

D. Image Feature Extraction

A wide collection of image features, including the wavelet decomposition, and principal components have been tested for their effectiveness in separating different types of abnormalities [64]. The study based on continuous wavelet transform (CWT) has shown a good separability between the classes [65]. The continuous wavelet transform (CWT) of a function *f(t)* with respect to an analyzing ψ wavelet function, is defined as follows [66]:

$$Wf_{\psi}(b,a) = \frac{1}{\sqrt{a}} \int_{-\infty}^{\infty} f(t)\psi\left(\frac{t-b}{a}\right)dt \quad a > 0 \tag{4.1}$$

The parameter *b* is called the translation parameter. This parameter indicates the position or location of the wavelet function. The parameter *a* is called the dilatation parameter. The inverse of this parameter 1/ *a* can be regarded as a measure of frequency. This transform to be reversible the wavelet must satisfies the *admissibility condition*. That is.

$$C_{\psi} = \int_{-\infty}^{\infty} \frac{|\hat{\psi}(\omega)|^2}{|\omega|} dt < \infty \text{ Where } \hat{\Psi} \text{ is the Fourier transform of } \Psi \tag{4.2}$$

By changing *b* and *a*, the transform $Wf\psi(b,a)$ can be presented as a so-called time-scale plot. region (sub-image) search algorithm (RSA) that was developed in [64, 65] was used to find the wavelength ranges corresponding to the highest levels of separation. Fig. 17 illustrates the corresponding time-scale plot using the Morlet wavelet and the RSA algorithm

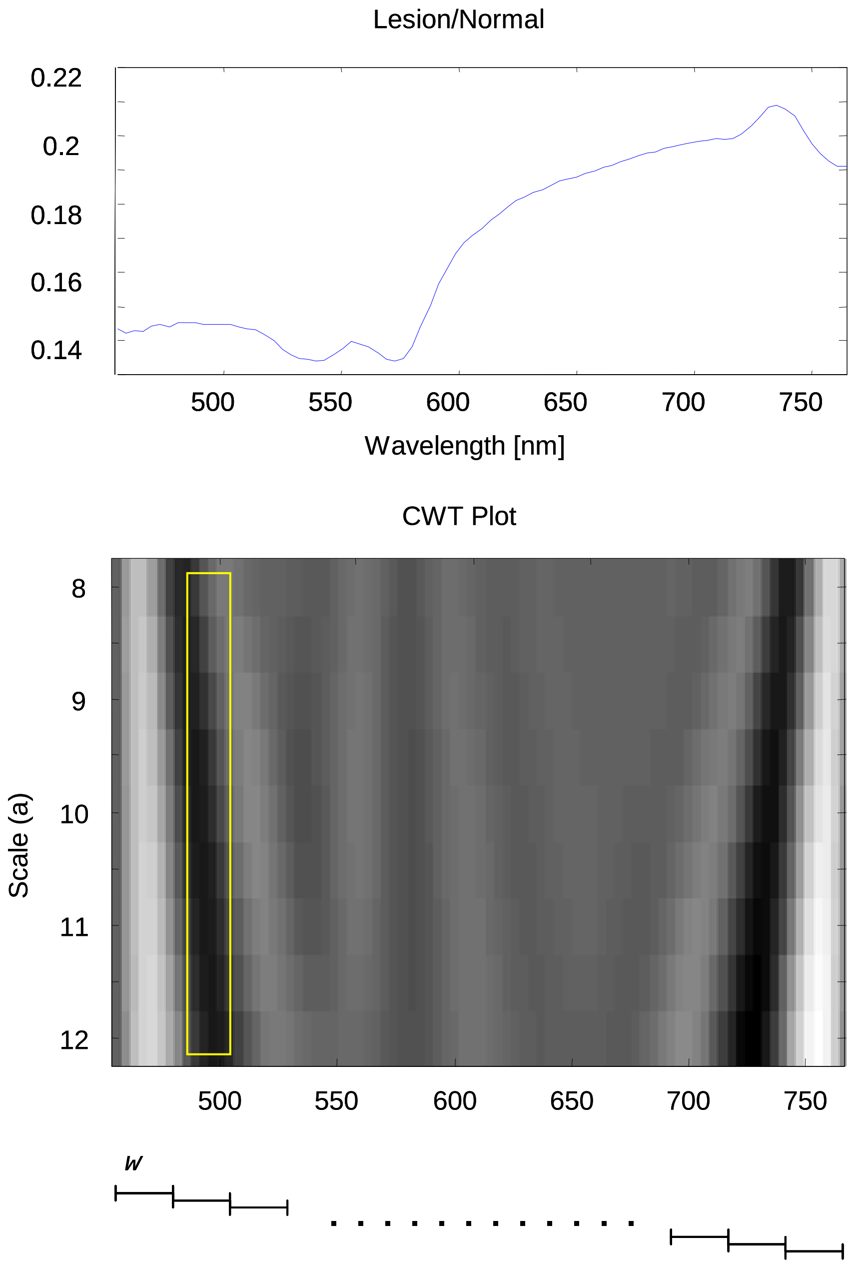
Lesion/Normal

CWT Plot

Fig 17. Time-scale plot using the Morlet wavelet and the RSA algorithm.

E. Feature Selection and Conditioning

This stage of the image analysis involved identifying those image features that possessed relatively non-overlapping distributions for benign and cancerous cases. A genetic algorithm (GA) was used to find the most effective combination of extracted wavelet features. This GA is capable of searching a high dimensional feature space efficiently. Basically, the GA maximizes a fitness function, corresponding to the product of the Fisher distance (FD) and the area under the Receiver Operating Characteristic (ROC) curve in our case, by carrying out three stochastic types of searching operations: population, crossover, and mutation [67]. Fig. 18 shows the steps involve in genetic algorithm. The Fisher distance is given by

$$FD=|\mu_b - \mu_c|/(\sigma_b^2 + \sigma_c^2)^{1/2} \tag{4.3}$$

where μ_b and μ_c denote the class means, and σ_b and σ_c are the class variances. The ROC curve shows sensitivity versus (1 – specificity) [68]. Sensitivity indicates the percentage of correctly identified positives (true positives) and specificity the correctly identified negative cases, thus (1 – specificity) is the false alarm rate. A ROC area close to one indicates a good separation of benign and cancerous cases. Before feeding the above effective image features into a classifier, they were passed through two conditioning modules to remove their correlation and to reduce their dimensionality to one. For convenience this combined image feature is termed CIF.

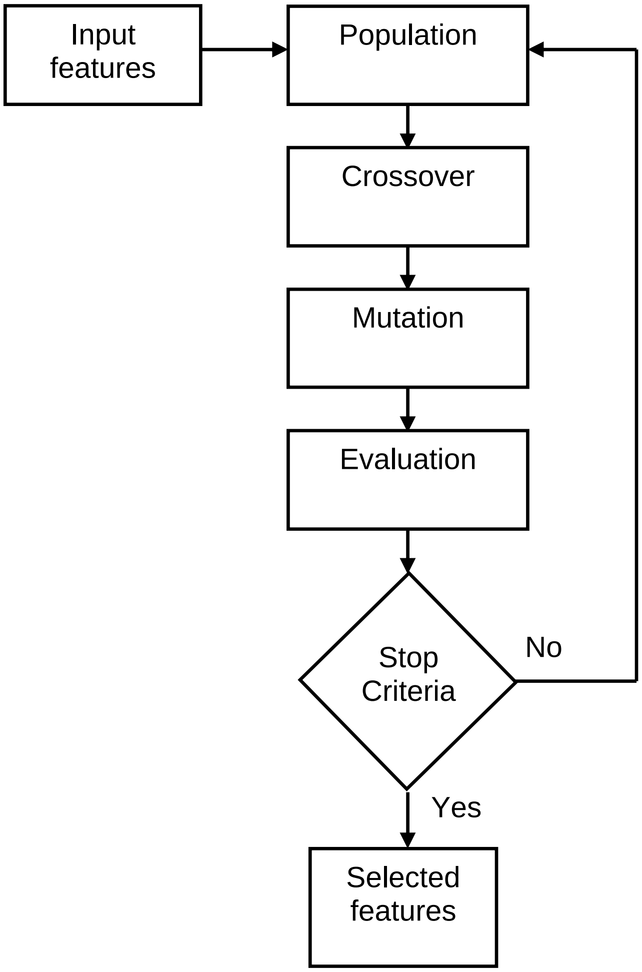

Fig. 18.Genetic algorithm.

The correlation among the features was removed by the following transformation

$$\underline{\hat{x}} = A_1(\underline{x} - \underline{\mu}) \tag{4.4}$$

where $\underline{x}$ denotes a feature vector whose components are the selected features, $\underline{\mu}$ indicates the mean vector and

$$A_1=(\underline{e}_1, \underline{e}_2, \ldots \underline{e}_q)^t \tag{4.5}$$

where $\underline{e}_i$'s represent the eigenvectors of the covariance matrix, and q the number of features. Covariance matrix Cov and mean vector $\underline{\mu}$ are computed as:

$$Cov = \frac{1}{n}\sum_{p=1}^{n}\left(\underline{x}_p - \underline{\mu}\right)\left(\underline{x}_p - \underline{\mu}\right)^t \tag{4.6}$$

$$\underline{\mu} = \frac{1}{n}\sum_{p=1}^{n}\underline{x}_p \tag{4.7}$$

The reduction of the dimensionality greatly helps the classification task. The dimensionality was reduced by first computing the between-class scatter matrix (S_B) and the within-class scatter matrix (S_w) as follows [69]:

$$S_W = \sum_{i=1}^{Ci} S_i \tag{4.8}$$

$$S_B = \sum_{i=1}^{Ci} n_i\left(\underline{\mu} - \underline{\mu}_i\right)\left(\underline{\mu} - \underline{\mu}_i\right)^t \tag{4.9}$$

where

$$S_i = \sum_{\underline{\hat{x}} \in Ci}\left(\underline{\hat{x}} - \underline{\mu}_i\right)\left(\underline{\hat{x}} - \underline{\mu}_i\right)^t \tag{4.10}$$

and $\underline{\mu}_i$ is the mean of the ith class C_i and n_i the number of samples in that class. The following separability measure J was then used to reduce the dimensionality

$$J = Trace\ (S_W^{-1} S_B) \tag{4.11}$$

This was achieved by multiplying the transpose of the non-zero eigenvector A_2 of the matrix ($S_W^{-1}S_B$) with the feature vectors. Since it is a two-class problem, there existed only one non-zero eigenvalue. The set of features are combined into one feature generating the same separability measure *J*. For a two-class problem this final feature has a dimensionality one.

F. Classification

Statistical Bayes classifiers [69-72] were designed to classify two subgroups of classes at a time within the pigmented group and the non-pigmented group. This procedure was repeated for the all the subgroups until the desired categories were achieved. Fig. 19 illustrates the procedure for the pigmented lesions.

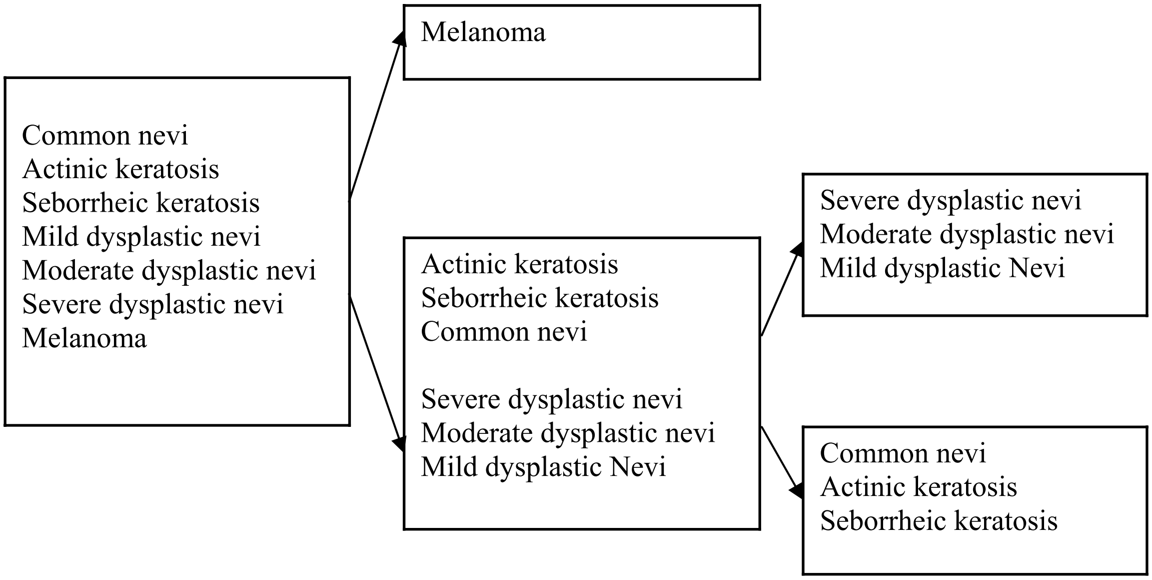

Fig. 19. Classification of the pigmented skin lesion.

For the pigmented lesion group, the first and most important classifier separates the malignant lesion subgroup (including invasive melanoma, melanoma in situ and) from the benign lesion subgroup (including actinic keratosis, seborrheic keratosis, common nevi), and precancerous subgroup (mild, moderate and severe dysplastic nevi).

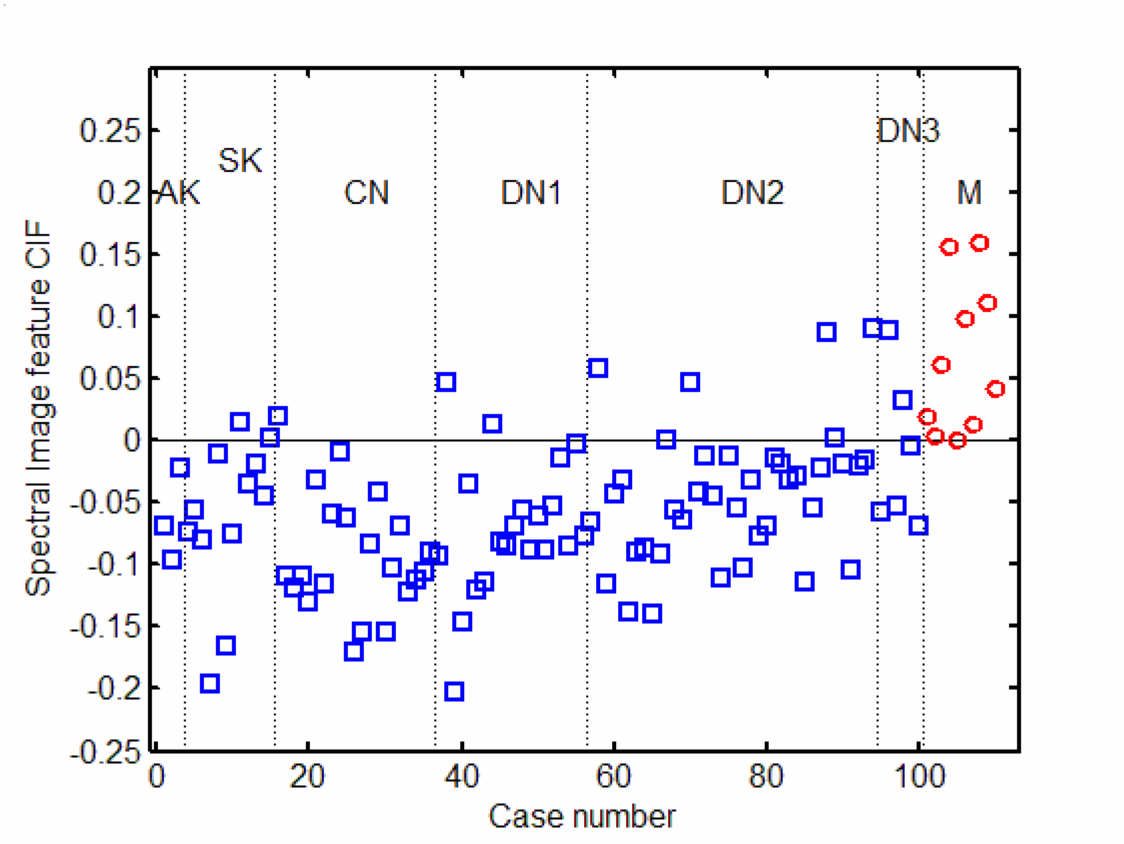

Fig. 20. Results of the first classifier for pigmented lesion: training dataset. This first classifier uses 110 lesions for training and 57 lesions for testing.

The Bayes decision rule for the minimization of the probability of error is as follows: for a feature vector x, decide class 1 if P(class 1 / x) > P(class 2 / x); otherwise decide class 2. Using our 1-dimension combine Image feature (CIF) and assuming a

Gaussian distribution, the decision rule simplifies to: decide class 1 if g(class 1) > g(class 2); otherwise, decide class 2. Where

$$g(\text{class } 1) = -\ln(\sigma_1) - (x_{CIF} - \mu_1)^2 / \sigma_1 \qquad (4.12)$$

and

$$g(\text{class } 2) = -\ln(\sigma_2) - (x_{CIF} - \mu_2)^2 / \sigma_2 \qquad (4.13)$$

$\mu_{1,}$ and μ_1 denotes the class means and σ_1 and σ_2 the class variances.

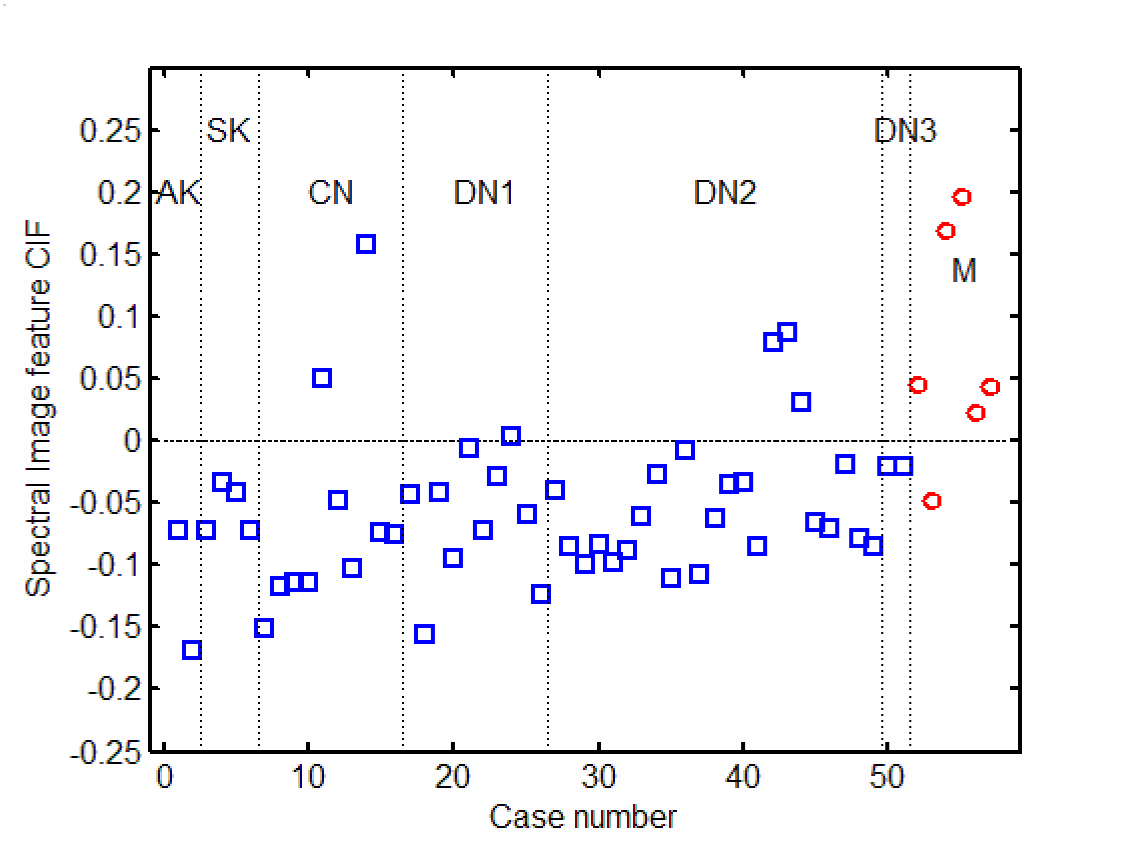

Fig. 21. Results of the first classifier for pigmented lesion: testing dataset.

As shown in Fig. 20. This classifier for the training data set performs with 100% sensitivity and 89% specificity. The Fig. 21 shows the scatter plot for the testing set with sensitivity of 83% and a specificity of 88%. The overall classification rates are 89% and 88% for the training and testing set, respectively.

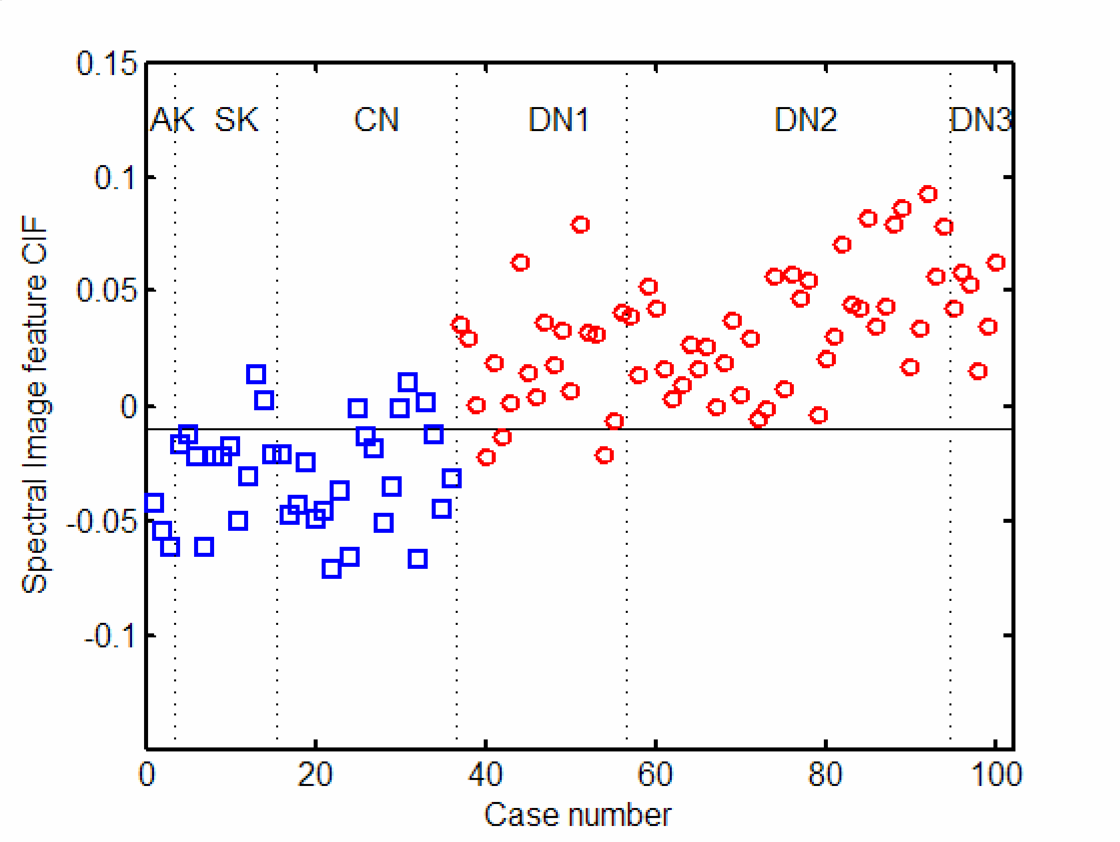

Fig. 22. Results of the second classifier for pigmented lesion: training dataset.

A second classifier was designed to distinguish the benign common nevi actinic keratosis and seborrheic keratosis from mild dysplastic nevi, moderate dysplastic nevi and severe dysplastic nevi. A total of 100 lesions were used for training and 51 lesions were for testing. The overall classification rates are 91% for the training set and 90% for the testing set. Figs. 22 and 23 show the scatter plots for the training and testing set respectively.

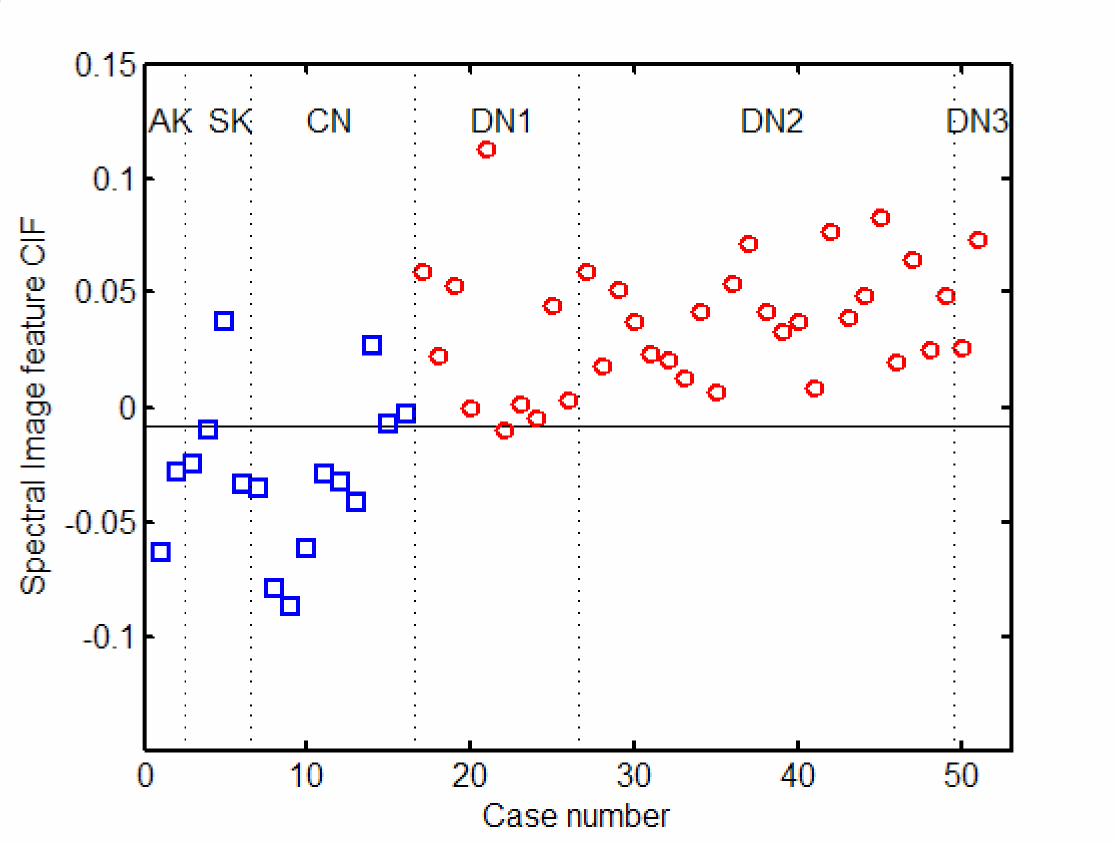

Fig. 23. Results of the second classifier for pigmented lesion: testing dataset.

For the non-pigmented group. A single classifier separates basal cell carcinomas (BCC) and squamous cell carcinomas (SCC) from actinic keratosis (AK,) seborrheic keratosis (SK). A total of 53 lesions were used to train the classifiers and 25 lesions were used for testing. The designed classifier generated an overall classification rate of 95%

with 97% sensitivity and 91% specificity. The Figs. 24 and 25 show the classification results for non-pigmented lesion.

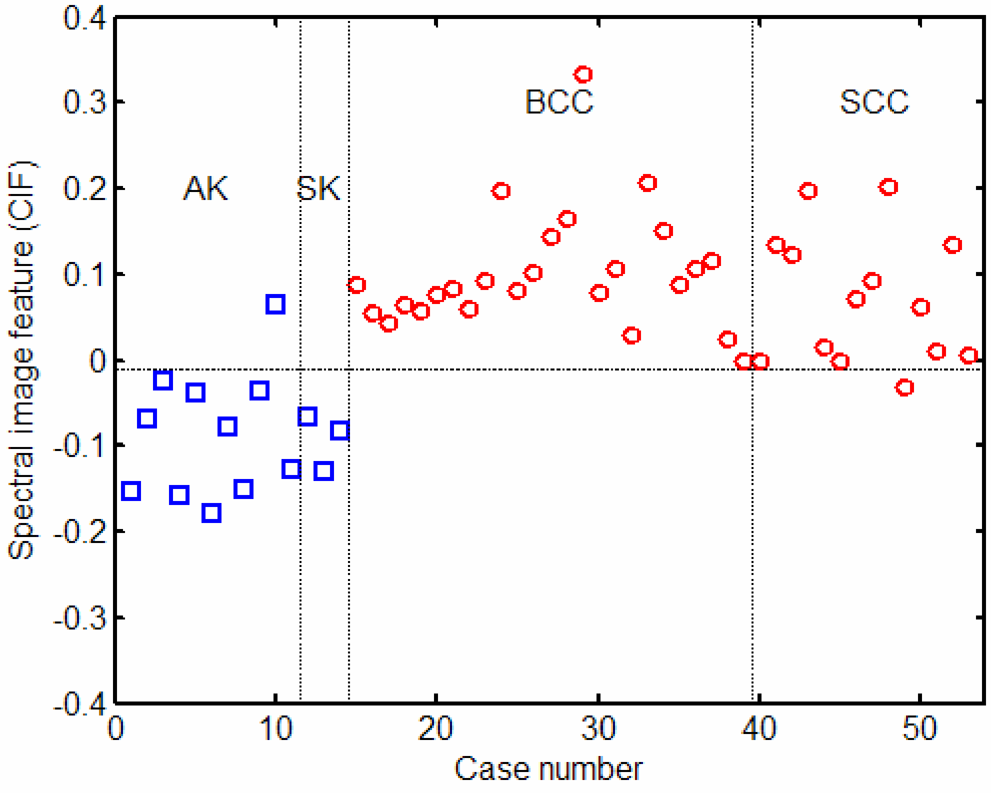

Fig. 24. Results of the design dataset for the non-pigmented lesions.

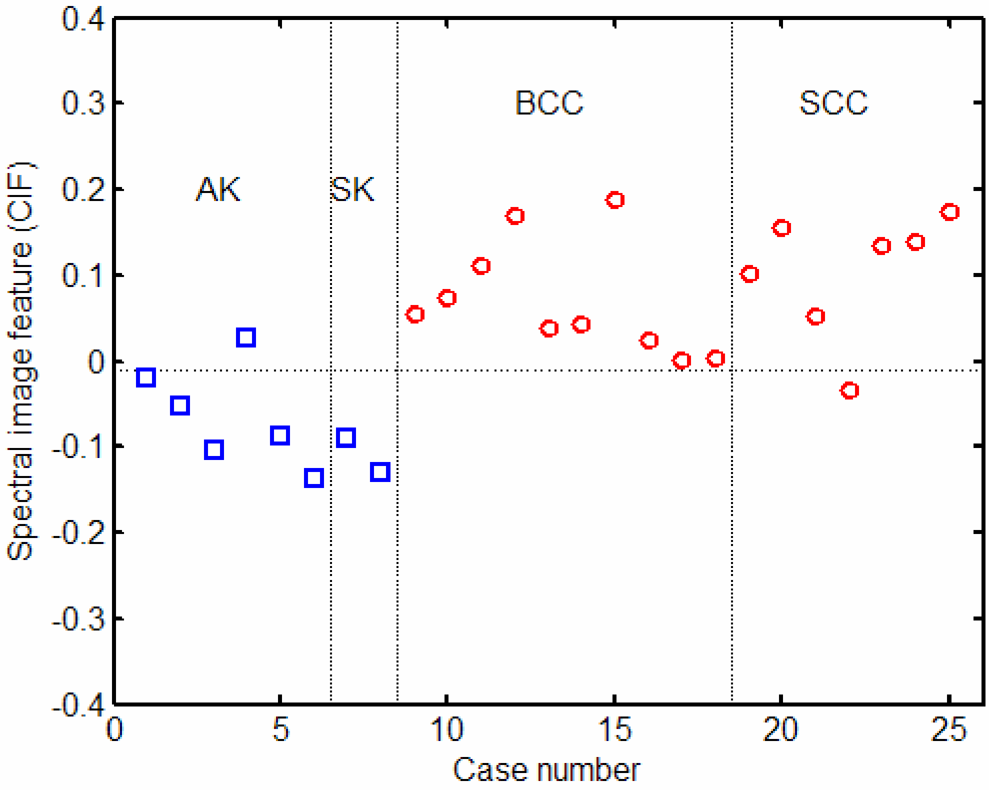

Fig. 25. Results of the testing dataset for the non-pigmented lesions.

CHAPTER V

ANALYSIS OF OPTICAL PROPERTIES OF SKIN LESIONS

In our second analysis, we computed the absorption spectra (μ_a) and the reduced scattering spectra (μ_s') from the *in-vivo* diffuse reflectance data and used them to extract appropriate physiological parameters of the skin lesions. This analysis was meant to provide an understanding of the physiological origins associated with different types of skin abnormalities.

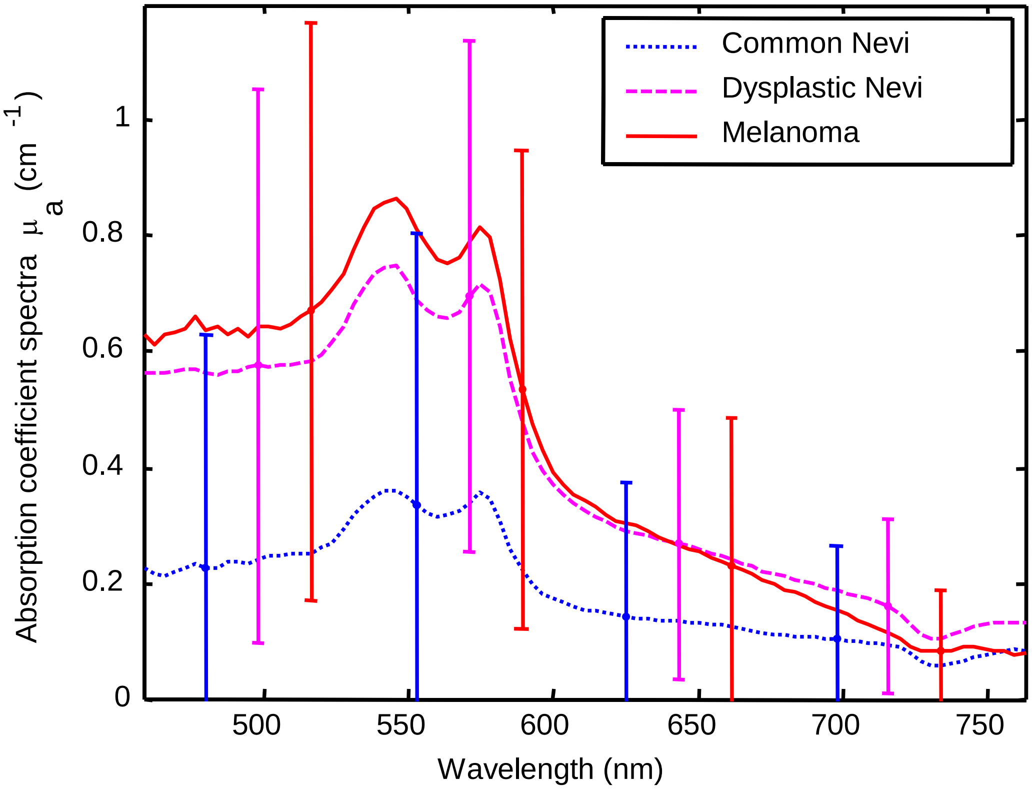

Fig. 26. Absorption coefficient spectra of common nevi, dysplastic nevi and melanoma.

Figs. 26 and 27 show the average absorption coefficient spectra (μ_a) and reduced scattering coefficient spectra (μ_s') for melanoma, dysplastic and common nevi, respectively [73]. The error bars represent the standard deviations for each type of skin abnormality.

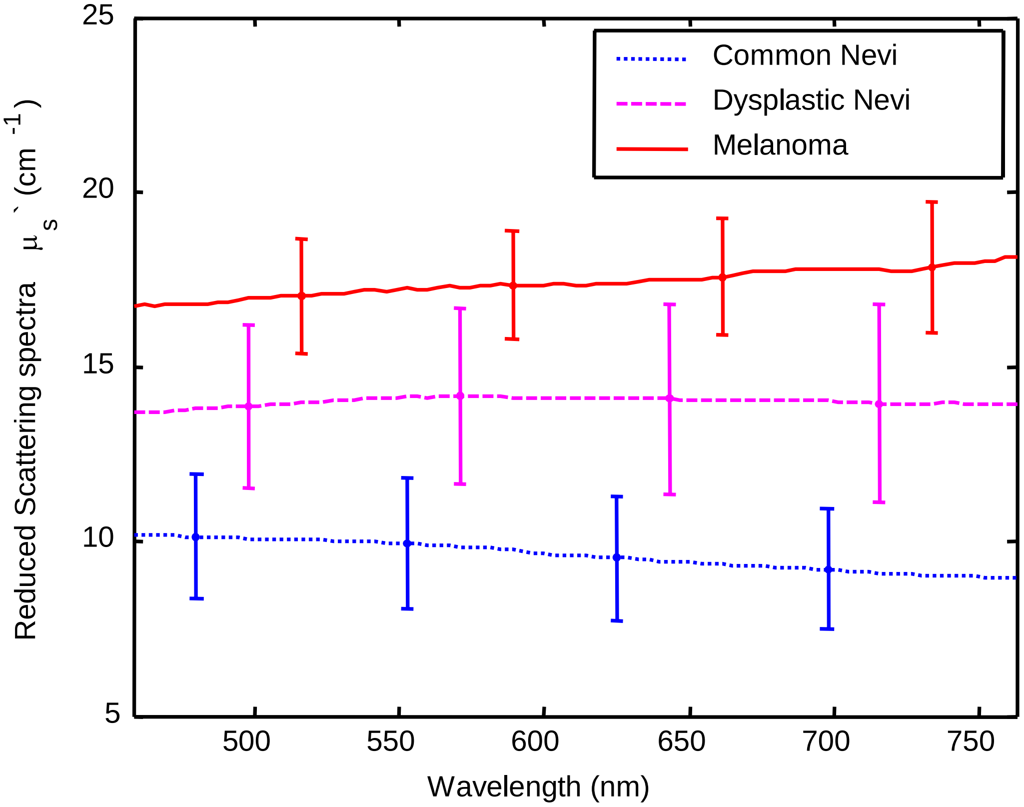

Fig. 27. Reduced scattering coefficient spectra of common nevi, dysplastic nevi and melanoma.

The absorption coefficient spectra can be used to extract the following physiological parameters: concentration of hemoglobin (C_{hb}), concentration of oxygenated (C_{ox}) and deoxygenated hemoglobin (C_{de}), and oxygen saturation of hemoglobin (SO_2). These parameters are considered important because they are believed to be related to the disease state of lesions [74-76]. the reduced scattering spectra can be used to estimated the size distribution $f(\varphi)$, where φ is the scatterer size. The steps involved in the analysis are as shown in Fig. 28.

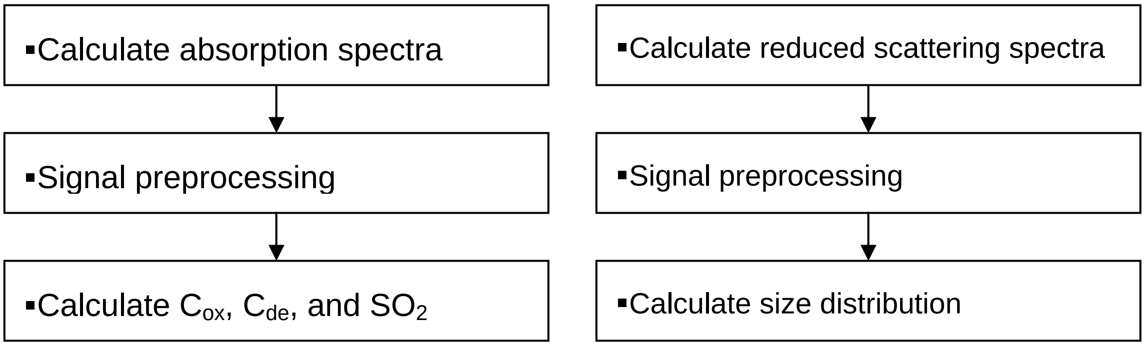

Fig. 28. Steps involved in the analysis of physiological properties.

We assume that cell nuclei are the primary scatterers [77, 78]. Since these scatterers are considerably larger than the wavelengths under consideration, the more general Mie theory rather than Rayleigh theory must be used [79]. The reduced scattering coefficient is a function of the wavelength, the diameter of the cell nuclei, and the relative refractive index. For this reason, one can estimate the size distribution $f(\varphi)$ from the reduced scattering spectra using the inverse Mie theory [80-82].

$$\mu_s'(\lambda) = \frac{C_s}{4}\int_0^\infty Q_s(\phi,n,\lambda)\left[1-g(\phi,n,\lambda)\right]f(\phi)\pi\phi^2 d\phi \tag{5.1}$$

where $\mu_s'(\lambda)$ is the reduced scattering spectrum of the tissue; C_s is the total volume concentration of the scatterers; $Q_s()$ is the scattering efficiency; ϕ is the diameter of the scatterers; n is the relative index of refraction of the scatterers, λ is the wavelength, $g()$ is the scattering anisotropy [83]. It has been shown that the diameter of a non-dysplastic cell nuclei is typically 5–10 μm, whereas dysplastic nuclei can be as large as 20 μm across in epithelial lesions [62]. This can explain the higher scattering coefficient for the melanoma cases shown in Fig. 27.

Table III and IV summaries the results for the physiological parameters extracted from the optical properties presented in [65, 73]. This table shows that the cancerous lesions have lower oxygen saturation than the benign lesions. The lower oxygen saturation in cancer lesions can be related to several factors including (1) malignant progression (2) tumor death and necrosis, (3) intratumoral hemorrhage with blood stagnation, (4) abnormal blood supply and distribution and (4) metabolic abnormalities [75, 84]. This table also indicates that the expected value of the size distribution of scatterers E[φ] in the malignant cases is larger than in the benign cases.

Table III. Average concentration of hemoglobin and oxygen saturation.

	C_{hb} (mM)	StO_2 (%)
Common Nevi	0.00220 +/- 0.00144	0.49 +/- 0.13
Dysplastic Nevi	0.00348 +/- 0.00141	0.48 +/- 0.12
Melanoma	0.00456 +/- 0.00264	0.44 +/- 0.18

Table IV. Average size nuclei for pigmented and non pigmented lesion.

Parameter	Non-pigmented lesion		Pigmented lesions	
	Carcinoma	Keratosis	Dysplastic nevi	Common nevi
$E[\phi]$ [μm]	20.4 ±7.5	6.3 ± 5.5	15.7 ± 8.8	9.0 ±4.8

The optical parameters plotted in Figs. 26 and 27 and the physiological parameters listed in Table III and IV indicate a general common trend in each category of skin lesion. However, the similar mean values or the large (overlapping) variances existing among different categories implies that due to the biological variability, accurate classification of skin lesions based on a single physiological or resulting optical parameter will be almost impossible. A comprehensive approach which combines most or all of the “effective” features would provide a feasible way to achieve accurate diagnosis. This explains that measuring and signal processing of the diffuse reflectance spectra of skin.

Table V. Relative difference of the concentration of hemoglobin and oxygen saturation compared with the normal surrounding skin.

	ΔC_{hb}	ΔSO_2 (%)
Common Nevi	-0.00121	-0.035 +/- 0.22
Dysplastic Nevi	0.00117	-0.06 +/- 0.26
Melanoma	0.00134	-0.16 +/- 0.25

The optical properties of human skin vary significantly between individuals, dependent on race, age, and sun exposure. In order to have a better understanding of the relationship between of the physiological parameters extracted from the optical properties it is important to subtract the information for the surrounding normal skin. The Table V shows the relative difference of the concentration of hemoglobin and oxygen saturation by subtracting the parameters from the skin lesion from the ones from the surrounding skin. The melanoma case presented significantly lower oxygen saturation (-16%) than the surrounding healthy skin, which is indication of hypoxia.

CHAPTER VI

MEMS-BASED OBLIQUE-INCIDENCE OPTICAL SPECTROSCOPIC ENDOSCOPY

A. Esophageal Endoscopy

Endoscopy is the main tool for diagnosing esophageal cancer. It is a procedure involving the use of a gastroscope, which is one type of endoscope specially designed for gastroenterology applications. A gastroscope consists of a flexible tube with a light guide for illumination, an objective lens and camera for video capture, an air/water nozzle for cleaning the lens, and an instrument channel to accept a series of accessories for biopsy and other treatment purposes (Fig. 29). Once inserted into the GI tract, the flexible tube can be rotated along its axis and its distal end can have a 2-way angulation for efficient examination of esophagus and other portions of the GI tract. A biopsy can be taken through the endoscope for histology to determine whether cancer is present.

Fig. 29. End view of the GI endoscope.

B. Side-view Probe Design and Fabrication

For OIDRS measurements, the sensor probe needs to be in contact with the tissue surfaces of interest. As shown in Fig. 30, the skin probe assumes a “front viewing” configuration, in which the sensor head is in line with the direction of the source/collection fiber bundles. All the collection fibers remain straight and thus can be arranged in a dense manner with suitable spacing for capturing the spatial distribution of the diffuse reflectance. To accommodate the 45^o bending of the source fiber for oblique incidence, a large outer dimension of the probe ($15\times10\times150$ mm^3) is used to prevent sharp bending of the source fibers. For *in-vivo* skin testing, the “front viewing” configuration and the relatively large size of the probe are desirable for hand-held applications. However, for inner-body applications (e.g. esophagus), this configuration and dimension of sensor probe becomes an issue. First, to conduct effective and efficient *in-vivo* measurement inside human body, the OIDRS probe has to be mounted onto a medical endoscope for manipulation and targeting. Current medical endoscope can only accept tool attachments with 2~5 mm in diameter. The current OIDRS probe is too bulky for this purpose. Second, while the “front viewing” configuration is ideal for skin applications, it will be difficult to use it to conduct *in-vivo* measurements in the tight inner-body cavities. A “side viewing” configuration is preferred, in which the sensor head is oriented in a perpendicular position with respect to the axis of the fiber bundles (Fig. 31). However, this inevitably requires a sharp 90^o turn for all the collection fibers within very tight space, which would cause significant light loss and leakage (thus cross-talk between adjacent collection channels) and also possible mechanical fracture of the fibers.

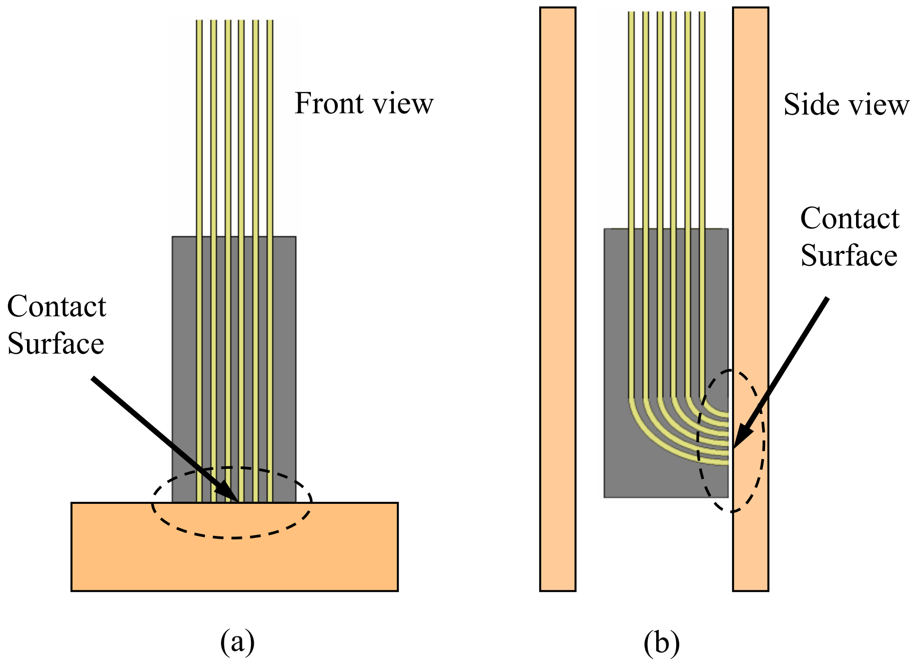

Fig. 30. Schematic of OIDRS probe configuration: (a) front viewing and (b) side viewing.

To solve this problem, we have applied MEMS technologies to develop a prototype of a new miniaturized “side-viewing” OIDRS probe [85]. As shown in Fig. 31, the new probe design consists of three substrates. The first substrate serves as the positioning device to guide the source fiber for a 45^{o} oblique `incidence. To avoid the detrimental effects of direct sharp bending of the collection fiber array, a second substrate with microfabricated polymer waveguides is used for collecting the diffuse reflectance. The four side walls of curved polymer waveguides are coated with highly reflective layers to prevent possible light leakage and cross-talk of the waveguides (Fig. 32). To interface the waveguides to OIDRS image capture and processing setup, a third substrate with bulk-etched V-groves is used to align the straight interconnection fiber bundles with exactly the same pitch of that of the polymer waveguides (Fig. 32). The assembled sensor head and the complete probe are shown in Figs. 33 and 34, respectively. The outer dimension of the probe head is 5×5×30mm^3. In contrast, the previously developed "front viewing" skin probe has an outer dimension of 15×10×150mm^3.

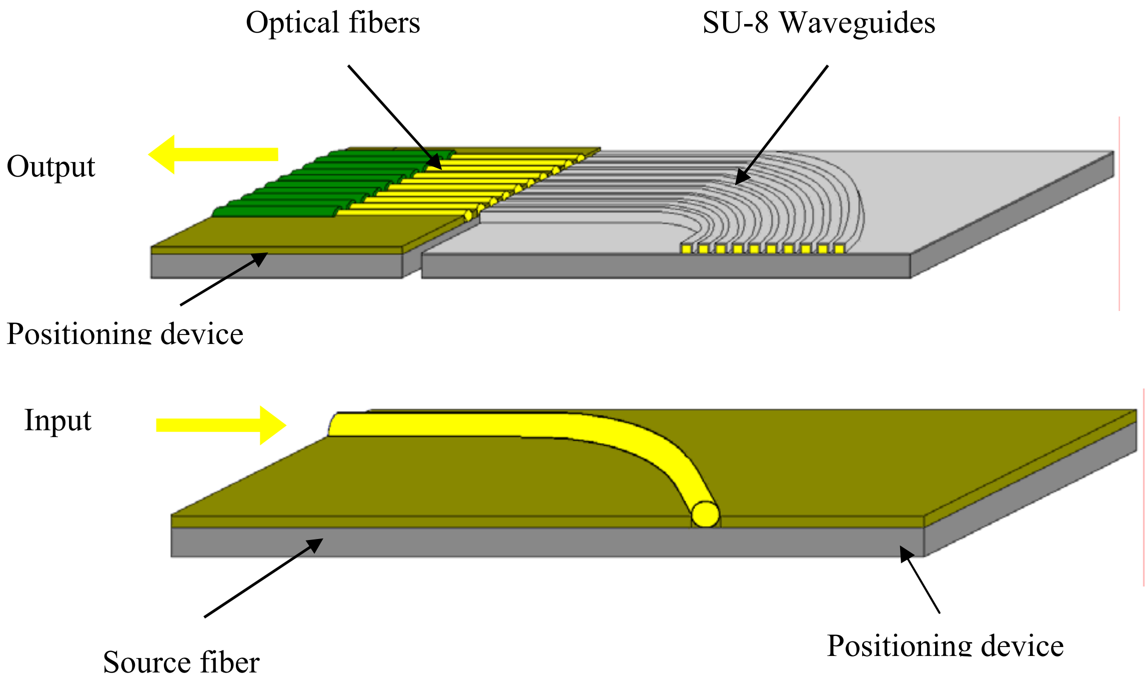

Fig. 31. Schematic of the "side-viewing" OIDRS probe assembly.

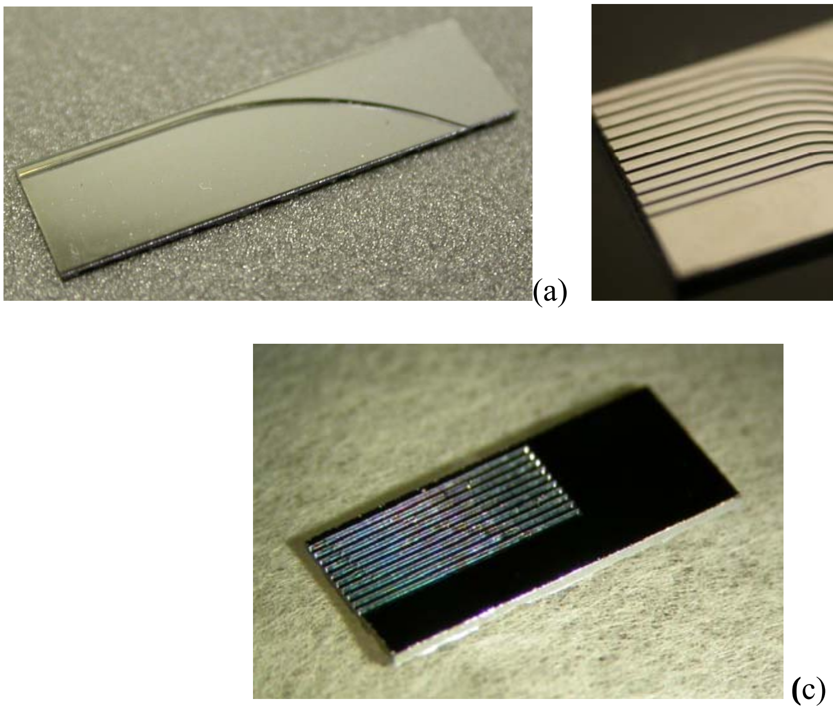

Fig. 32. Micromachined silicon positioning substrates for the OIDRS probe: (a) Source fiber guide; (b) Collection waveguide substrates; and (c) Interconnection fiber guide.

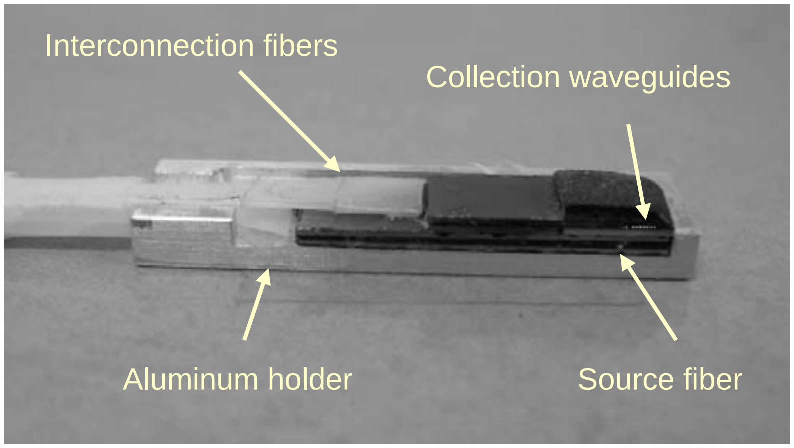

Fig. 33. An assembled probe head.

08 13 20

Fig. 34. Complete probe.

C. Ex-Vivo OIDRS Measurement of Esophageal Lesions

The fabricated “side viewing” OIDRS probe was connected to a previously developed image acquisition system and calibrated using a standard liquid phantom with known optical properties. After the calibration, the entire OIDRS system was used to conduct ex-vivo measurement of fresh esophageal biopsy samples at the Barrett’s Esophagus Endoscopy Unit of Mayo Clinic (Rochester, MN). Each sample is approximately ~7 to 8 mm in diameter (Fig. 35). A total of 20 samples were measured. The measurement was done at the center of the sample and within 5 minutes after the biopsy was performed. The samples were later histopathologically analyzed following the standard procedure at Mayo Clinic. The 20 esophageal samples were found to consist of 8 benign, 6 low dysplastic, 4 highly dysplastic and 2 cancerous lesions.

Fig. 35. Esophageal biopsy sample.

Fig. 36 illustrates the average OIDRS data (after normalization by the light source) for each type of lesions. The collected data was used to design two classifiers. The first one separates benign and low dysplastic from high dysplastic and cancerous lesions. The second classifier distinguishes benign lesions from low dysplastic ones. Due to its small number, cancerous cases were combined with the high dysplastic ones.

D. Classification of Esophageal Lesions

Because of the limited number of samples, a bootstrap-based Bayes classifier [86] was used for each group based on the effective features for that group. The leave-one-out method was used for testing. Using this method, one sample from a lesion group was left out, and the bootstrap samples were generated separately for each class using the remaining samples.

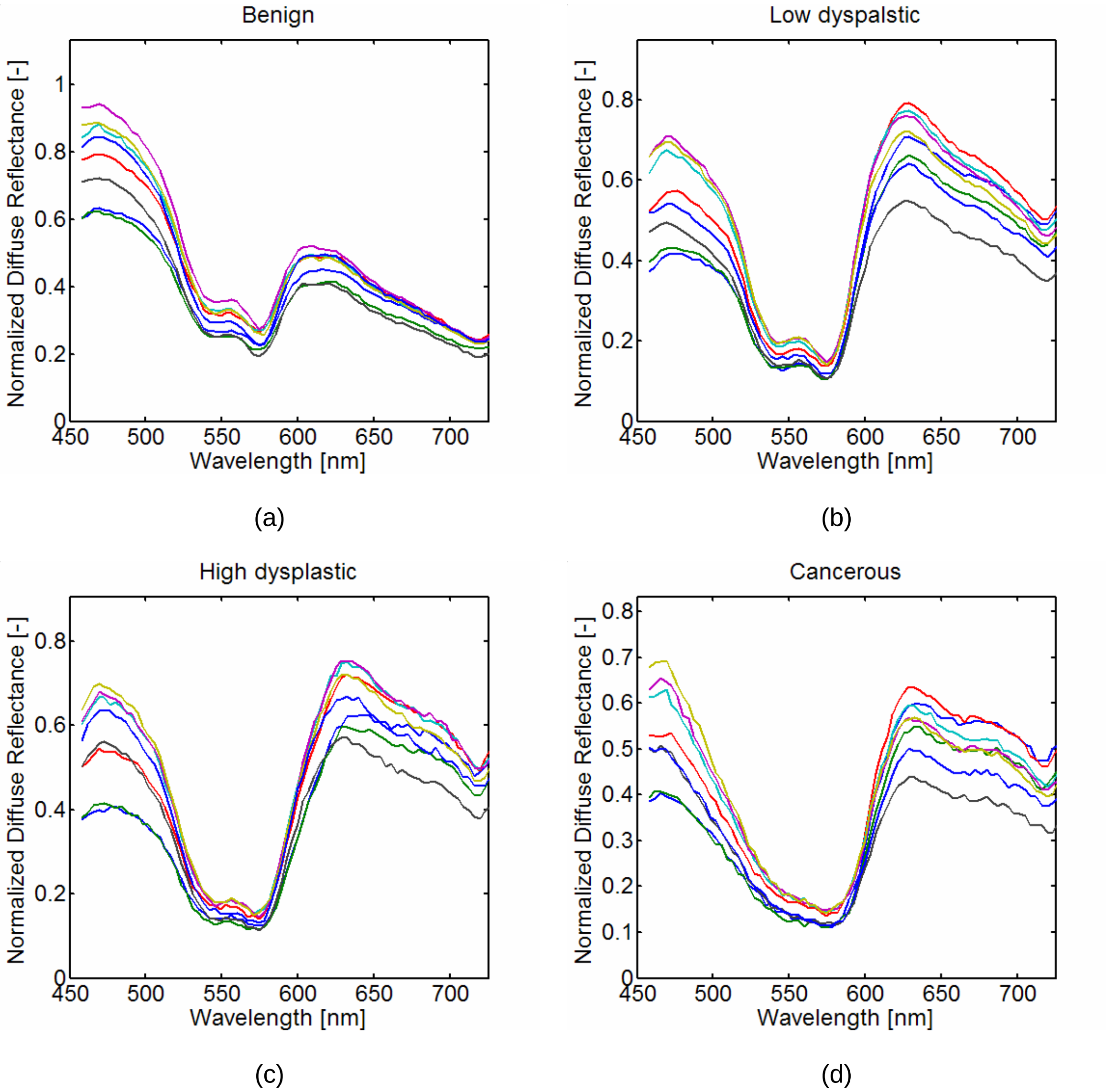

(a) (b) (c) (d)

Fig. 36. Average spatio-spectra OIDRS image from the fresh esophageal biopsy samples. (a) benign; (b) low dysplastic; (c) high dysplastic and (d) cancerous.

The classifier was tested with the left-out sample, and the classification (hit or miss) was recorded. The procedure was repeated by reinserting the removed sample, taking out a different sample, and regenerating new bootstrap samples, until each of the lesion samples had been individually removed and the classifier tested with all of the left-out samples. Both designed classifiers generated a classification rate of 100% (Figs. 37 and 38).

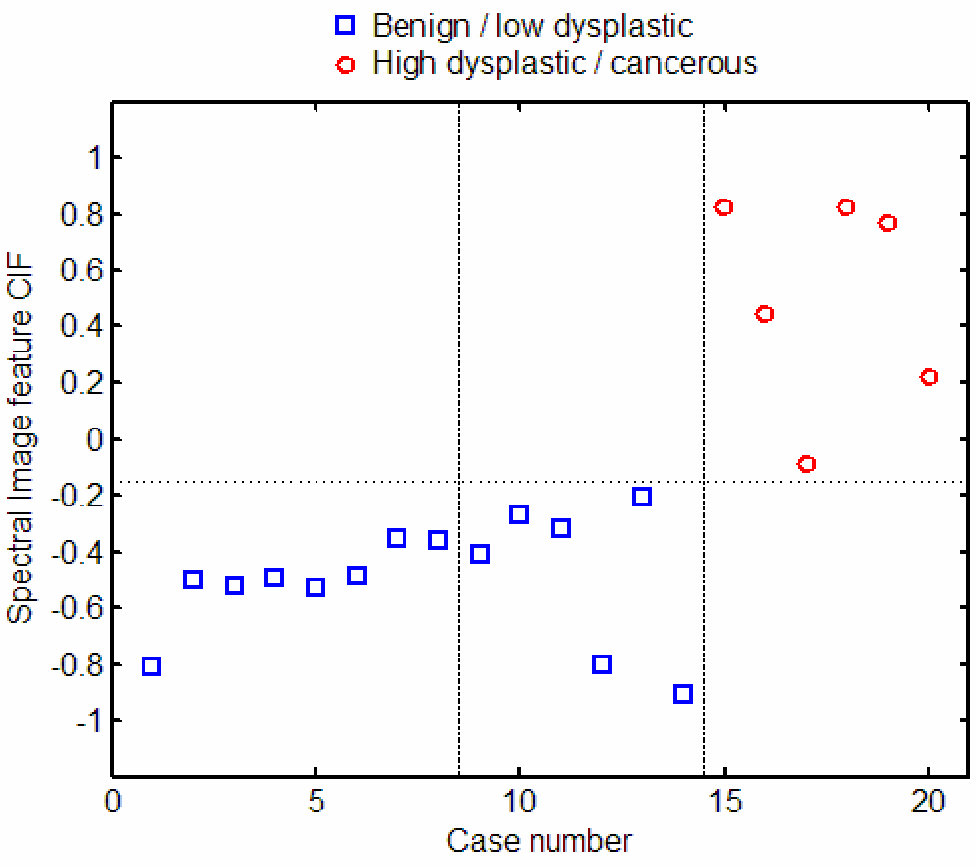

Fig. 37. Classification results of esophageal biopsy samples: benign/low dysplastic vs. high dysplastic/cancerous.

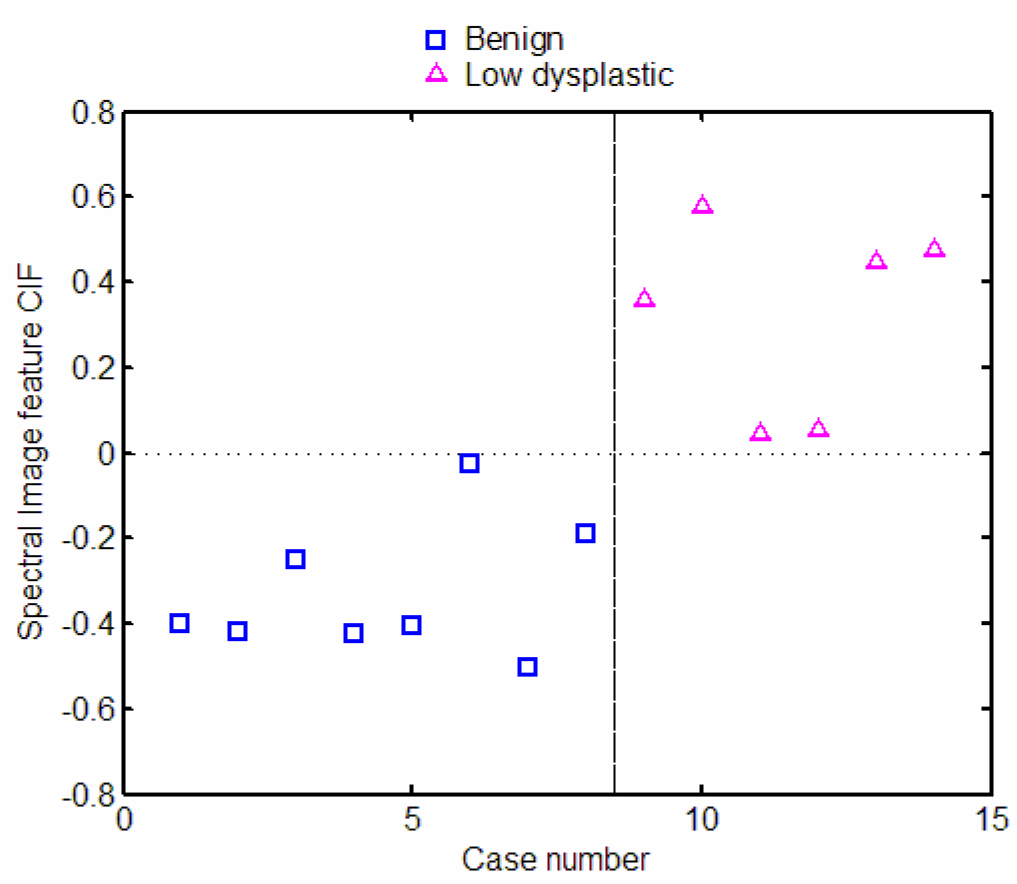

Fig. 38. Classification results of esophageal biopsy samples: benign vs. low dysplastic.

E. Ex-Vivo Optical Properties

The reduced scattering and absorption coefficient spectra were calculated from each sample. Figs. 39 and 40 show the average optical properties for the benign, low dysplastic and high dysplastic/cancerous cases. It shows that a higher average scattering coefficient spectra for the high dysplastic and cancerous cases than for low dysplastic and benign ones. The higher scattering coefficient for the group form by the high dysplastic and cancerous cases can be explained by the larger average effective size of the scattering centers. Enlarged nuclei are primary cellular indicators of cancer, dysplasia and cell in most human tissues. The absorption spectra show lower oxygen saturation for the malignant lesion than the benign ones. The lower oxygen saturation can be related to several factors including: tumor death and necrosis; abnormal blood supply and distribution; and metabolic abnormalities [75].

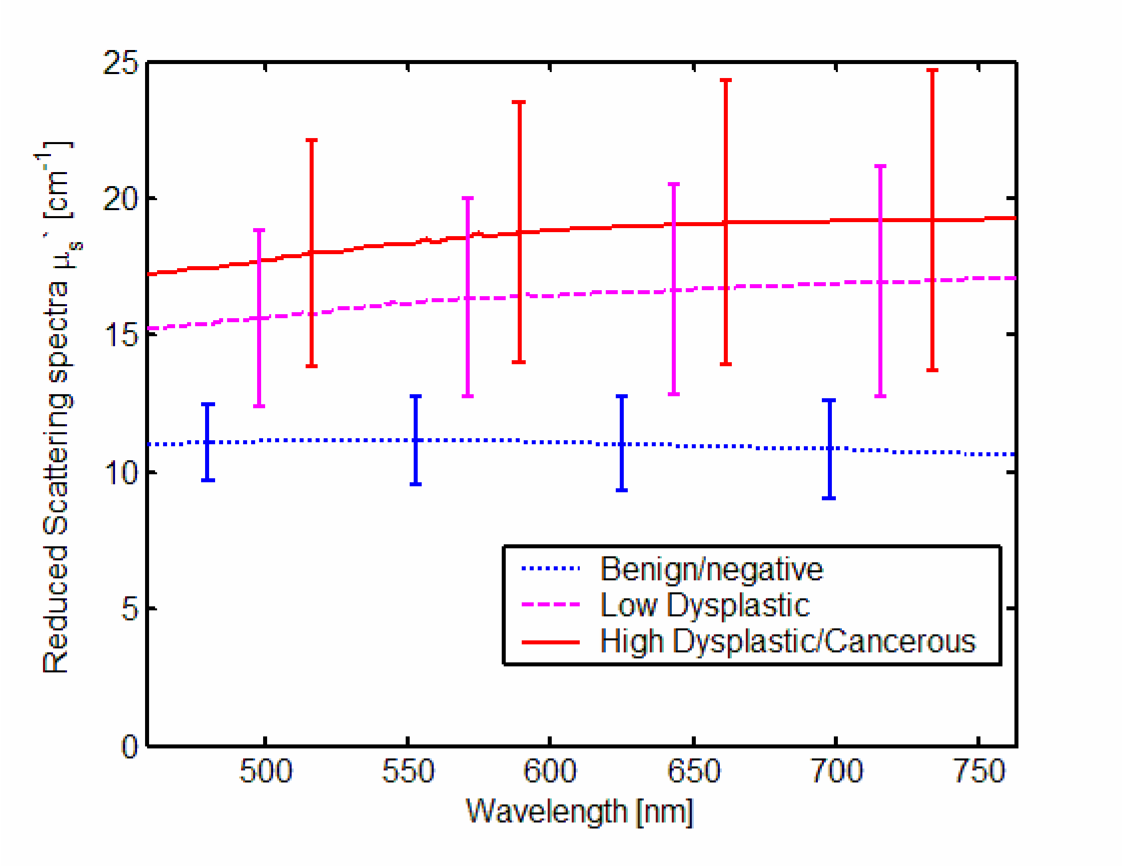

Fig. 39. Average reduced scattering absorption coefficient spectra, low dysplastic and high dysplastic/cancerous esophageal biopsy samples.

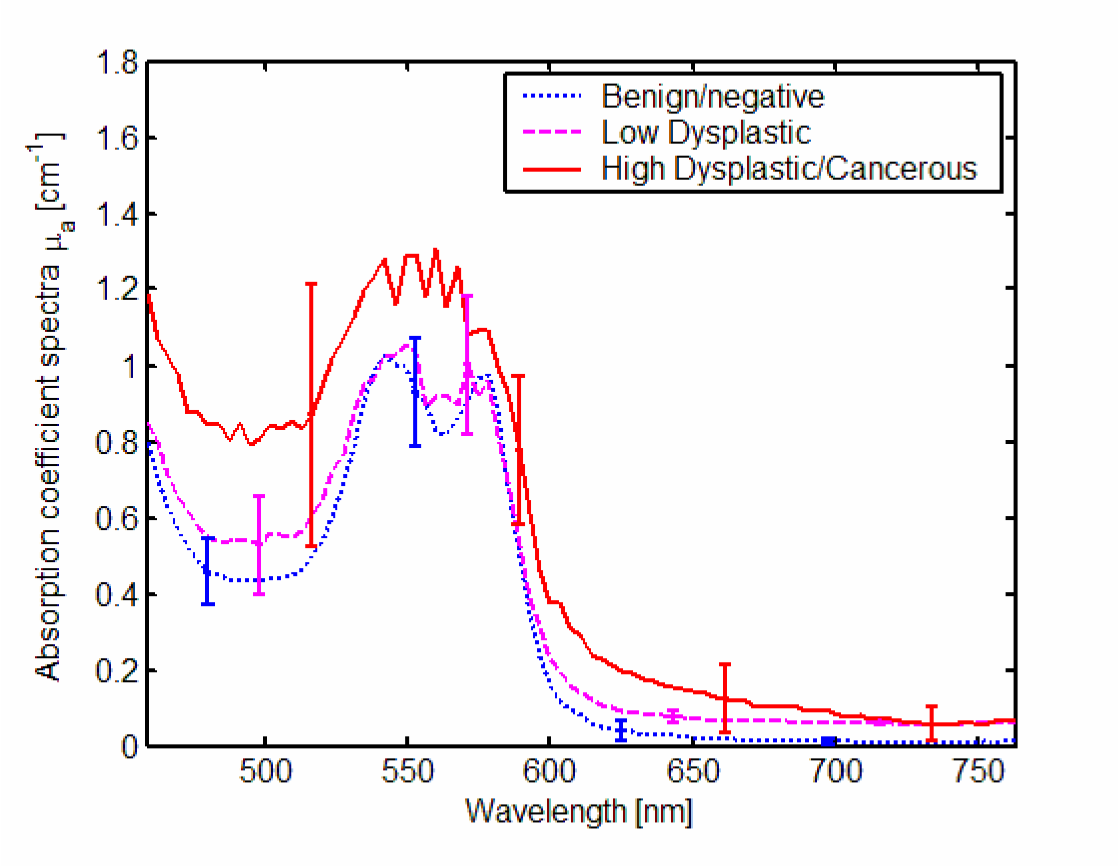

Fig. 40. Average absorption coefficient spectra, low dysplastic and high dysplastic/cancerous esophageal biopsy samples.

CHAPTER VII

SUMMARY AND CONCLUSIONS

An oblique incidence diffuse reflectance spectroscopy system has been developed and tested for non-invasive optical detection of epithelial cancer. Two micro-machined sensor probes has been designed and developed using micromachining technology. The first prone was designed for skin applications and the second one for esophageal applications. The device miniaturization and fabrication precision provided by micromachining ensure reliable and repeatable high performance of the probe. The results indicate that it is reliable for use to estimate the optical properties of the different types of tissues. The data from skin lesion was collected *in-vivo*. Several statistical classifiers were designed to separate cancerous skin lesions from the benign or precancerous counterparts. The classifier designed for the non-pigmented skin group separates carcinoma from the benign lesion with overall 97% sensitivity and 91% specificity and classification rate of 95%. The first statistical classifiers designed for pigmented skin lesion separates malignant melanoma from the benign and precancerous lesions with a performance of 100% sensitivity and 89% specificity for the training set and sensitivity of 83% and a specificity of 88% for the testing set. The second classifier was designed to separate the benign lesion form the precancerous one with an overall classification rates of 91% and 90% for the training and testing sets respectively. The second probe was developed with side-view capability. This probe was tested with ex-vivo esophageal lesion. Two classifiers were designed for this part of the study. The first one distinguishes benign and low dysplastic from high dysplastic and cancerous lesions. The second classifier separates benign lesions from low dysplastic ones. Both classifiers performed with a classification rate of 100%. The information provided by this system can potentially be used to assist the photodynamic therapy, and *in-vivo* and non-invasive diagnosis skin, esophageal and other organs pathologies.

REFERENCES

[1] D. Elder, R. Elenitsas, C. Jaworsky, and B. Johson, *Lever's Histopathology of the Skin*. 8th edition. Philadelphia, Lippincott-Raven, 1997, pp. 5-50, 617-746.

[2] American Cancer Society. Cancer Facts & Figures 2008. [cited Aug. 1, 2008]. [Online]. Available: http://www.cancer.org/docroot/STT/STT_0.asp.

[3] M. L. Williams and R. W. Sagebiel, "Melanoma risk factors and atypical moles," *The Western Journal of Medicine*, vol. 160, pp. 343-350, 1994.

[4] B. R. Masters, G. Gonnord, and P. Corcuff, "Three-dimensional microscopic biopsy of in vivo human skin: a new technique based on a flexible confocal microscope," *Journal of Microscopy*, vol. 185, pp. 329-338, 1997.

[5] Barrett's Esophagus. [cited Jun. 10, 2008]. [Online]. Available: http://www.mayoclinic.com/health/barretts-esophagus.

[6] V. P. Wallace, J. C. Bamber, D. C. Crawford, R. J. Ott, and P. S. Mortimer, "Classification of reflectance spectra from pigmented skin lesions, a comparison of multivariate discriminant analysis and artificial neural networks," *Physics in Medicine & Biology*, vol. 45, pp. 2859-2871, Oct. 2000.

[7] L. M. McIntosh, R. Summers, M. Jackson, H. H. Mantsch, J. R. Mansfield, M. Howlett and N. Crowson, J. W. Toole, "Towards non-invasive screening of skin lesions by near-infrared spectroscopy," *Journal of Investigative Dermatology*, vol. 6, pp. 75-87, Jan. 2001.

[8] S. Sigurdsson, P. A. Philipsen, L. K. Hansen, J. Larsen, M. Gniadecka, and H. C. Wulf, "Detection of skin cancer by classification of raman spectra," *IEEE Transactions on Biomedical Engineering* , vol. 51, pp. 1784-1793, Oct. 2004.

[9] M Gniadecka, P. A. Philipsen, S. Sigurdsson, S Wessel, O. F. Nielsen, D. H. Christensen, J. Hercogova, K. Rossen, H. K .Thomsen, R. Gniadecki R, L. K. Hansen, and H. C. Wulf, "Melanoma diagnosis by raman spectroscopy and neural networks: structure alterations in proteins and lipids in intact cancer tissue," *Journal of Investigative Dermatology*, vol. 122, pp. 443-449, Feb. 2004.

[10] C. J. Lynn, I. S. Saidi, D. G. Oelberg, and S. L. Jacques, "Gestational age correlates with skin reflectance in newborn infants of 24-42 weeks gestation," *Biol. of the Neonate*, vol. 64, pp. 69-75, 1993.

[11] M. Moncrieff, S. Cotton, E. Claridge, and P. Hall, "Spectrophotometric intracutaneous analysis: a new technique for imaging pigmented skin lesions," *British Journal of Dermatology*, vol. 146, no. 3, pp. 448-445, 2002

[12] V. P. Wallace, J. C. Bamber, D. C. Crawford, R. J. Ott, and P. S. Mortimer, "Classification of reflectance spectra from pigmented skin lesions, a comparison of multivariate discriminant analysis and artificial neural networks," *Physics in Medicine and Biology*, vol. 45, pp. 2859-2871, 2000.

[13] L. M. McIntosh, R. Summers, M. Jackson, H. H. Mantsch, J. R. Mansfield, M. Howlett, A. N. Crowson, and J. W. Toole, "Towards non-invasive screening of

skin lesions by near-infrared spectroscopy," *Journal of Investigative Dermatology*, vol. 116, pp. 175-181, 2001.

[14] S. Tomatis, M. Carrra, A. Bono, C. Bartoli, M. Lualdi, G. Tragni, A. Colombo, and R. Marchesini, "Automated melanoma detection with a novel multispectral imaging system: results of a prospective study," *Physics in Medicine and Biology*, vol. 50, pp. 1675-1687, 2005.

[15] D. Arifler, R. A. Schwarz, S. K. Chang, and R. Richards-Kortum. "Reflectance spectroscopy for diagnosis of epithelial precancer: mmodel-based analysis of fiber-optic probe designs to resolve spectral information from epithelium and stroma," *Applied Optics*, vol. 44, pp. 4291-4305, 2005.

[16] P. R. Bargo, S. A. Pral, T. T. Goodell, R. A. Sleven, G. Koval, G. Blair, and S. L. Jacques, "In vivo determination of optical properties of normal and tumor tissue with white light reflectance and an empirical light transport model during endoscopy," *Journal of Biomedical Optics*, vol. 10, 034018, May 2005.

[17] B. Mayinger, P. Horner, M. Jordan, C. Gerlach, Dipl.Phys. T. Horbach, W. Hohenberger, and E. G. Hahn, "Endoscopic fluorescence spectroscopy in the upper GI tract for the detection of GI cancer: initial experience," *The American Journal of Gastroenterology*, vol. 96, no. 9, pp 2616-2621, Sep. 2001.

[18] I. Georgakoudi, B. C. Jacobson, J. Van Dam, V. Backman, M. B. Wallace, M. G. Muller, Q. Zhang, K. Badizadegan, D. Sun, G. A. Thomas, L. T. Perelman, and M. S. Feld, "Fluorescence, reflectance, and light-scattering spectroscopy for

evaluating dysplasia in patients with Barrett's esophagus," *Gastroenterology*, vol. 120, no. 7, pp. 1620-1629, 2001.

[19] R. S. Dacosta, B. C. Wilson, and N. E. Marcon. "Light-induced fluorescence endoscopy of the gastrointestinal tract." *Gastrointest. Endosc. Clin. North Am.*, vol 10, pp. 37-69. 2000.

[20] R. S. Dacosta, B. C. Wilson, and N. E. Marcon, "New optical technologies for earlier endoscopic diagnosis premalignant gastrointestinal lesions," *Journal of Gastroenterology and Hepatology*, vol. 17, pp. S85–S104, 2002.

[21] R. J. Nordstrom, L. Burke, J. M. Niloff, and J. F. Myrtle,. Identification of cervical intraepithelial neoplasia (CIN) using UV-excited fluorescence and diffuse-reflectance tissue spectroscopy. *Lasers Surg. Med*, vol. 29 (2), pp. 118-127, 2001.

[22] Y. N. Mirabal, S. K. Chang, E. N. Atkinson, A, Malpica, M. Follen, and R. Richards-Kortum, "Reflectance spectroscopy for in vivo detection of cervical precancer," *Journal of Biomedical Optics*, vol. 7, no. 4, pp. 587-594, Oct. 2002.

[23] N. Ramanujam, M. F. Mitchell, A. Mahadevan, S. Warren, S. Thomsen, E. Silva, and R. Richards-Kortum,. In vivo diagnosis of cervical intraepithelial neoplasia using 337-nm-excited laser-induced fluorescence. *Proceedings of the National Academy of Sciences*, vol. 91, no. 21, pp. 10193-10197, 1994.

[24] A. Nath, K. Rivoire, S. Chang, , L West, S. B. Cantor, K. Basen-Engquist, K. Adler-Storthz, D. D Cox, E.N Atkinson, G. Staerkel, C. MacAulay, R. Richards-

Kortum, and M. Follen, “A pilot study for a screening trial of cervical fluorescence spectroscopy,” *International Journal of Gynecological Cancer*, vol. 14, no. 6, pp. 1097-1107, Nov. 2004

[25] K. S. Johnson, D. W. Chicken, D. C. Pickard, A. C. Lee, G. Briggs, M. Falzon, I. J. Bigio, M. R. Keshtgar, and S. G. Bown,. “Elastic scattering spectroscopy for intraoperative determination of sentinel lymph node status in the breast,” *Journal of Biomedical Optics*, vol. 9, no. 6, pp. 1122-1128, Nov. 2004.

[26] S. Fantini, S. A. Walker, M. A. Franceschini, M. Kaschke, P. M. Schlag, and K. T. Moesta, “Assessment of the size, position, and optical properties of breast tumors in vivo by noninvasive optical methods,” *Applied Optics*, vol. 37 (10), pp. 1982-1989, 1998.

[27] P. J. Tadrous, J. Siegel, P. M. French, S. Shousha, N. Lalani, and G. W. Stamp, “Fluorescence lifetime imaging of unstained tissues: early results in human breast cancer,” *Journal of Pathology*, vol. 199, no. 3, pp. 309-317, 2003.

[28] R. Richards-Kortum and E. Sevick-Muraca, “Quantitative optical spectroscopy for tissue diagnosis,” *Annual Rev. Phys. Chem*. vol. 47, pp. 555-606, 1996.

[29] L.-H. Wang and S. L. Jacques, “Analysis of diffusion theory and similarity relations,” *in Proc. of SPIE vol*. 1888, pp. 107-116, Sep, 1993.

[30] C. R. Simpson, M. Kohl, M. Essenpreis, and M. Cope, “Near-infrared optical properties of ex vivo human skin and subcutaneous tissues measured using the

Monte Carlo inversion technique," *Physics in Medicine and Biology*, vol. 43 2465-2478, 1998.

[31] A. Kienle and M. S. Patterson, "Determination of the optical properties of turbid media from a single Monte-Carlo simulation," *Physics in Medicine and Biology*, vol. 41, 2221-2227, 1996.

[32] L. V. Wang and H.-i Wu, *Biomedical Optics: Principles and Imaging*, New York: Wiley-Interscience, 2007.

[33] M. S. Patterson, B. C. Wilson and D. R. Wyman, "The propagation of optical radiation in tissue I. Models of radiation transport and their application," *Lasers in Medical Science*, vol. 6, no 2, pp. 155-168, Jun. 1991.

[34] L. H. Wang and S. L. Jacques, "Use of a laser beam with an oblique angle of incidence to measure the reduced scattering coefficient of a turbid medium," *Applied Optics*, vol. 34, no. 13 , pp. 2362-2366, May. 1995.

[35] S. -P. Lin, L. Wang, S. L. Jacques, and F. K. Tittel, "Measurement of tissue optical properties by the use of oblique-incidence optical fiber reflectometry," *Applied Optics*, vol. 36, no. 1, pp. 136-143, Jan. 1997.

[36] B. C. Wilson and G. A. Adam, "Monte Carlo model for the absorption and flux distributions of light in tissue," Medical Physics, vol.10, 824-830, 1983.

[37] S. T. Flock, B. C. Wilson, D. R. Wyman, and M. S. Patterson, "Monte-Carlo modeling of light-propagation in highly scattering tissues I: model predictions

and comparison with diffusion-theory," *IEEE Transactions Biomedical Engineering*, vol. 36, pp. 1162-1168, 1989.

[38] S. A. Prahl, M. Keijzer, S. L. Jacques, and A. J. Welch, "A Monte-Carlo model of light propagation in tissue," *in Proc. of SPIE Dosimetry of Laser Radiation in Medicine and Biology*, vol. IS 5, pp. 102-111, 1989.

[39] A. Sassaroli, C. Blumetti, F. Martelli, L. Alianelli, D. Contini, A. Ismaelli, and G. Zaccanti, "Monte-Carlo procedure for investigating light propagation and imaging of highly scattering media," *Applied Optics*, vol. 37, no. 31, pp. 7392-7400, Nov. 1998.

[40] E. Okada, M. Firbank, M. Schweiger, S. R. Arridge, M. Cope, and D. T. Delpy, "Theoretical and experimental investigation of near-infrared light propagation in a model of the adult head," *Applied Optics*, vol. 36, pp. 21-31, 1997.

[41] L.-H. Wang, S. L. Jacques, and L.-Q. Zheng, "MCML—Monte Carlo modeling of photon transport in multi-layered tissues," *Computer Methods and Programs in Biomedicine*, vol. 47, no. 2, pp. 131-146, Jul. 1995.

[42] L.-H. Wang, W. R. Chen, and R. E. Nordquist, "Optimal beam size for light delivery to absorption-enhanced tumors buried in biological tissues and effect of multiple beam delivery: a Monte Carlo study," *Applied Optics*, vol. 36, no. 31, pp. 8286-8291, Nov. 1997.

[43] A. Kienle and M. S. Patterson, "Determination of the optical properties of turbid media from a single monte-carlo simulation," *Physics in Medicine and Biology*, vol. 41, no. 10, pp. 2221-2227, Oct. 1996.

[44] I. Lux and L. Koblinger, *Monte Carlo Particle Transport Methods: Neutron and Photon Calculations* Boca Raton FL,CRC Press, 1991.

[45] L. V. Wang and G. Liang, "Absorption distribution of an optical beam focused into a turbid medium," *Applied Optics*, vol. 38, no. 22. pp. 4951-4958, Aug. 1999.

[46] A. Garcia-Uribe, K. C. Balareddy, J. Zou and L. V. Wang, "Micromachined fiber optical sensor for *in-vivo* measurement of optical properties of human skin," *IEEE Sensors Journal*, vol. 8, no. 10, pp. 1698-1703, Oct. 2008.

[47] A. Garcia-Uribe, J.-M. Hong, J. Zou and L. V. Wang. "Micromachined Oblique Incidence Reflectometry (OIR) Probe for Skin Cancer Detection," *in Proc. of IEEE Solid-State Sensors, Actuators and Microsystems Conference, Transducers '07*, Lyon, France. 2007, pp. 1099-1102.

[48] G. Marquez, L.-H. Wang, S.-P. Lin, J. A. Schwartz, and S. L. Thomsen, "Anisotropy in the absorption and scattering spectra of chicken breast tissue," *Applied Optics*, vol. 37, no. 4, pp. 798–805, Feb. 1998.

[49] H. C. Van de Hulst, *Light Scattering by Small Particles*, New York: Dover Publications, 1981.

[50] S. Prahl, Optical Properties Spectra [Online]. Available: http://omlc.ogi.edu/

spectra.

[51] M. Larsson, H. Nilsson, and T. Stromberg. "In vivo determination of local skin optical properties and photon path length by use of spatially resolved diffuse reflectance with applications in laser Doppler flowmetry," *Applied Optics*, vol. 42, pp. 125-134, Jan. 2003.

[52] A. N. Bashkatov, E. A. Genina, V. I. Kochubey and V. V. Tuchin, "Optical properties of human skin, subcutaneous and mucous tissues in the wavelength range from 400 to 2000 nm," *J. Phys. D: Appl. Phys.* vol. 38, pp.2543-2555, Aug. 2005.

[53] C. R. Simpson, M. Kohl, M. Essenpreis and M. Cope, "Near-infrared optical properties of ex-vivo human skin and subcutaneous tissues measured using the Monte Carlo inversion technique," *Physics in Medicine & Biology*, vol. 43, pp. 2465-2478, Sep. 1998.

[54] J. S. Dam, C. B. Pedersen, T. Dalgaard, P. E. Fabricius, P. Aruna, and S. Andersson-Engels, "Fiber-optic probe for noninvasive real-time determination of tissue optical properties at multiple wavelengths," *Applied. Optics*, vol. 40, pp. 1155-1164, Mar. 2001.

[55] H. Liu, D. A. Boas, Y. Zhang, A. G. Yodh, and B. Chance, "Determination of optical properties and blood oxygenation in tissue using continuous NIR light," *Physics in Medicine & Biology*, vol. 40, pp. 1983-1993, Nov. 1995.

[56] V. P. Wallace, J. C. Bamber, D. C. Crawford, R. J. Ott, and P. S. Mortimer, "Classification of reflectance spectra from pigmented skin lesions, a comparison of multivariate discriminant analysis and artificial neural networks," *Physics in Medicine & Biology*, vol. 45, pp 2859-2871, Oct. 2000.

[57] L. M. McIntosh, R. Summers, M. Jackson, H. H. Mantsch, J. R. Mansfield, M. Howlett, N. Crowson, and J. W. Toole, "Towards non-invasive screening of skin lesions by near-infrared spectroscopy," *Journal of Investigative Dermatology*, vol. 6, pp. 75-87, Jan. 2001.

[58] S, Sigurdsson, P, A, Philipsen, L, K, Hansen, J, Larsen, M, Gniadecka, and H, C, Wulf, "Detection of skin cancer by classification of raman spectra," *IEEE Transactions on Biomedical Engineering*, vol. 51, Oct. 2004.

[59] M Gniadecka, PA Philipsen, S Sigurdsson, S Wessel, O. F. Nielsen, D. H. Christensen, J. Hercogova, K. Rossen, H. K .Thomsen, R. Gniadecki R, L. K. Hansen, and H. C. Wulf, "Melanoma diagnosis by raman spectroscopy and neural networks: structure alterations in proteins and lipids in intact cancer tissue," *Journal of Investigative Dermatology*, vol. 122, pp. 443-449, Feb. 2004.

[60] R. A. His, D. I. Rosenthal, and E. Glatstein, "Photodynamic therapy in the treatment of cancer: current state of the art," *Drugs*, vol. 57, pp. 725-734, May 1999.

[61] H. -W Wang, M. E. Putt, M. J. Emanuele, D. B. Shin, E. Glatstein, A. G. Yodh and T. M. Busch, "Treatment-induced changes in tumor oxygenation predict

photodynamic therapy outcome,” *Cancer Research*, vol. 64, pp. 7553-7561, Oct. 2004.

[62] L. T. Perelman, V. Backman, M. Wallace, G. Zonios, R. Manoharan, A. Nusrat, S. Shields, M. Seiler, C. Lima, T. Hamano, I. Itzkan, J. Vandam, J. M. Crawford, and M. S. Feld, “Observation of periodic fine structure in reflectance from biological tissue - a new technique for measuring nuclear size distribution,” *Physical Review Letters*, vol. 80, no. 3, pp. 627-630, Jan.1998.

[63] G. Marquez and L.-H. Wang, "White light oblique incidence reflectometer for measuring absorption and reduced scattering spectra of tissue-like turbid media," *Optics Express*, vol. 1, pp. 454-460, 1997.

[64] M. Mehrubeoglu, N. Kehtarnavaz, G. Marquez, M. Duvic, and L.-H. Wang, “Skin lesion classification using diffuse reflectance spectroscopic imaging with oblique incidence,” *Applied Optics*, vol. 41, no. 1, 182–192, Jan. 2002.

[65] A. Garcia-Uribe, N. Kehtarnavaz, G. Marquez, V. Prieto, M. Duvic, and L. V. Wang, “Skin cancer detection by spectroscopic oblique-incidence reflectometry: classification and physiological origins,” *Applied Optics*, vol. 43, no. 13, pp. 2643-2650, May 2004.

[66] J. Groswami, and A. K. Chan, *Fundamentals of Wavelets, Theory, Algorithms and Applications*, first edition, New York: Wiley Interscience Publication, 1999.

[67] H. Vafaie and K. Jong, "Genetic algorithms as a tool for feature selection in machine learning," *in Proc. of the Int'l Conference on Tools with Artificial Intelligence*, Arlington, VA, 1992, pp. 200-204.

[68] A. P. Bradley, "The use of the area under the ROC curve in the evaluation of machine learning algorithms," *Pattern Recognition*, vol. 30, no. 7, pp. 1145-1159, Jul. 1997.

[69] R. O. Duda, P. E. Hart, and D. G. Stork, *Pattern Classification*, 2nd ed., New York: Wiley Interscience, 2000.

[70] A. M. Zoubir, and B. Boashash, "The bootstrap and its applications in signal processing," *IEEE Signal Processing Magazine*, vol. 15, no 1, pp. 56-76, Jan. 1998.

[71] S. Theodoridis and K. Koutroumbas, *Pattern Recognition*, San Diego, CA: Academic Press, 1999.

[72] K. Fukunaga, *Introduction to Statistical Pattern Recognition*, second edition, New York: Academic Press, 1990.

[73] A. Garcia-Uribe, E. B. Smith, K. C. Balareddy, J. Zou, M. Duvic, V. Prieto and L. V. Wang "*In-vivo* characterization of optical properties of pigmented skin lesions including melanoma using oblique incidence diffuse reflectance spectroscopy," *Journal of Biomedical Optics*, to be submitted for publication.

[74] H. B. Stone, J. M. Brown, T. L. Phillips, and R. M. Sutherland, “Oxygen in human tumors: correlations between methods of measurement and response to therapy,” *Radiation Research*, vol. 136, no. 3, pp. 422-434, Dec. 1993.

[75] R. S. Cotran, V. Kumar and T. Collins. *Robbins Pathologic Basis of Disease*. 6th ed. Philadelphia: W. B. Saunders Company, 1999.

[76] S. Thomsen and D. Tatman “Physiological and pathological factors of human breast disease that can influence optical diagnosis,” *Annals of the New York Academy of Sciences*, vol. 838, no. 1 , pp. 171–193, Feb. 1998.

[77] J. R. Mourant, M. Canpolat, C. Brocker, O. Esponda-Ramos, T. M. Johnson, A. Matanock, K. Stetter, and J. P. Freyer, “Light scattering from cells: the contribution of the nucleus and the effects of proliferative status,” *Journal of Biomedical Optics*, vol. 5, pp. 131-137, 2000.

[78] J. R. Mourant, J. P. Freyer, A. H. Hielscher, A. A. Eick, D. Shen, and T. M. Johnson, *Applied Optics*, vol. 37, pp. 3586-3593, 1998.

[79] C. F. Bohren, and D. Huffman, *Absorption and Scattering af Light By Small Particles*, New York: John Wiley, 1983.

[80] H. B. Jiang, J. Pierce, J. Kao, and E. Sevick-Muraca, “Measurement of particle-size distribution and volume fraction in concentrated suspensions with photon migration techniques,” *Applied. Optics*, vol. 36, no. 15, pp. 3310-3318, May 1997.

[81] E. Sevick-Muraca, J. Pierce, H. B. Jiang, and J. Kao, "Photon-migration measurement of latex size distribution in concentrated suspensions," *AIChE Journal*, vol. 43, no. 3, pp. 655-664, 1997.

[82] H. Jiang, G. Marquez, and L.-H. Wang, "Particle sizing in concentrated suspensions by use of steady-state, continuous-wave photon migration techniques," *Optics Letters*, vol. 23, no. 5, pp. 394-396, Mar. 1998.

[83] H. C. van de Hulst, *Light Scattering by Small Particles*, New York: Dover Publications Inc., 1981.

[84] M. Hockel, K Schienger, B. Aral, M. Milze, U. Schaffer, and P. Vaupel, "Association between tumor hypoxia and malignant progression in advanced cancer of the uterine cervix," *Cancer Research*, vol. 56, pp. 4509-4515, Oct. 1996.

[85] A. Garcia-Uribe, K. C. Balareddy, J. Zou, A. Wojcik, L. V. Wang and K. K. Wang, "Micromachined side-viewing optical sensor probe for non-invasive detection of esophageal Cancers," *Sensors and Actuators A: Physical*, to be published.

[86] B. Efron and R, Tibshirani, "Bootstrap methods for standard error, confidence interval, and other measures of statistical accuracy," *Statistical Science*, vol. 1, no. 1, pp. 54-75, Feb. 1986.

VITA

Alejandro Garcia Uribe was born in Morelia, Mexico in 1976. He received his Bachelor of Science degree in electronics engineering from the Instituto Tecnológico de Morelia, Mexico, in September of 1998. He entered the Electrical and Computer Engineering Department at Texas A&M University in 2000 and received his Master of Science degree in electrical engineering in August of 2002.

Alejandro Garcia Uribe may be reached at 214 Zachry Engineering Center, College Station, Texas 77843-3128.